

PROJECT REPORT ENTITLED

**RECENT CHANGES IN TROPICAL PACIFIC:
ASSOCIATION WITH CLIMATE CHANGE**

FOR PARTIAL FULFILMENT OF
MASTER OF TECHNOLOGY
IN
ATMOSPHERIC SCIENCE

SUBMITTED BY

Mr. NITIN U. PATIL

UNDER THE GUIDANCE OF

Dr. ASHOK KARUMURI
SCIENTIST - E



CENTRE FOR CLIMATE CHANGE RESEARCH
INDIAN INSTITUTE OF TROPICAL METEOROLOGY
PUNE

SUBMITTED TO

DEPARTMENT OF ATMOSPHERIC AND SPACE SCIENCES
UNIVERSITY OF PUNE, PUNE

APRIL 2011

ACKNOWLEDGEMENT

*With great pleasure, I express my deep sense of gratitude to my guide **Dr. Ashok Karumuri**, Scientist E, Centre for Climate Change Research Division, Indian Institute of Tropical Meteorology (IITM), Pune, for giving me an opportunity to do my project work under his guidance and supervision, and for his valuable suggestions and encouragement during the course of the work.*

*I express my sincere thanks to **Dr. B. N. Goswami**, Director, I.I.T.M, **Dr. R. Krishnan**, Scientist G and Head, Centre for Climate Change Research Division and **Dr. (Mrs.) P. S. Salvekar**, Co-ordinator, Academic Cell, I.I.T.M for providing necessary infrastructure facilities for doing my work in this esteemed institution.*

*I take this opportunity to thank **Dr. P. Pradeep Kumar** Head, Department of Atmospheric and Space Sciences, University of Pune, Pune for permitting me to do my project at IITM, Pune.*

*I am also thankful to **Dr. Roxy Mathew**, Scientist C and **Mr. Sabin T. P.**, Scientist B, CCCR Division, IITM, Pune for his constant inspiration and valuable help and to all members of the IITM CCCR group, who helped me throughout the course of my work.*

(Mr. NITIN PATIL)

CONTENTS

<i>Sr. No.</i>	<i>TITLE</i>	<i>Pg. No.</i>
1.	INTRODUCTION	1
2.	DATA AND METHODOLOGY	4
	2.1) Datasets used	4
	2.2) CMIP3 dataset overview	5
	2.3) Methodology	6
	a) <i>Empirical Orthogonal Function</i>	6
	b) <i>Partial Correlation</i>	8
3.	RESULTS	9
	3.1) Analysis of the 20C3M SST and comparison with observations for the period 1971-2000	9
	3.2) Models simulations in SRES A1B scenario.....	20
	3.3) Teleconnections with ISMR	30
	a) <i>Observations and Models in 20C3M</i>	30
	b) <i>Projections in SRESA1B scenario</i>	34
4.	SUMMARY AND CONCLUSIONS	38
5.	REFERENCES	41

1. INTRODUCTION

The Indian monsoon is one of the dominant tropical circulation systems in the general circulation of the atmosphere. Variability of rainfall during the monsoon season (June-September) has profound impacts on water resources, power generation, agriculture, economics and ecosystems in the country. The Sea Surface Temperature (SST) variability of the tropical Pacific has important implications for climate worldwide and primarily associated with El Niño-Southern Oscillation (ENSO) events. El Niño's are defined by warmer than normal sea surface temperatures in the eastern tropical Pacific, and are associated with anomalous atmospheric circulation patterns known as the Southern Oscillation. These coupled phenomena, together called ENSO (*Fig. 1.1a*), have been the subject of research since the late nineteenth century. ENSO phenomena are recognized as one of the most important interactions between the ocean and the atmosphere of the climate system (*Philander, 1990*). The El Niño/Southern Oscillation (ENSO) is the most important source of inter-annual variability of the Indian summer monsoon. The El Niño events (*Rasmusson and Carpenter, 1982; Philander, 1990*), which typically occur every 3–8 years or so, cause global effects on climate, for example on agriculture in India. However, the climate is changing with accelerated atmospheric warming since late 1970s. The signal is also seen in the ocean heat content (*Levitus et al., 2005*). In association with the climate change in 1970s, the tropical Pacific SST is also changing. A new phenomena recently referred to as the El Niño "Modoki" (*Ashok et al. 2007*), is characterized by warm SST anomaly in the central equatorial Pacific and a cold SST anomaly is observed in the western and eastern Pacific (*Fig. 1.1b*). El Niño "Modoki" (Modoki is Japanese for "similar, but different") (*Ashok and Yamagata, 2009*). Nonetheless, the increasing frequency of a new type of El Niño Modoki is due to global warming (*Ashok et al., 2007; Yeh et al., 2009*). The maximum SST anomaly (SSTA) persists in the central Pacific from the boreal summer through to the winter, modifying the atmospheric circulation and resulting indistinctly different global impacts (*Ashok et al., 2007; Yeh et al., 2009*). It is known that ENSO and ENSO Modoki generate atmospheric changes globally through teleconnections (*Ropelewski and Halpert, 1987; Aceituno, 1988; Trenberth et al., 1998; Diaz et al., 2001; Ashok et al., 2007;*

Yeh et al., 2009); it is beneficial to study its potential impacts on the Indian Summer Monsoon Rainfall.

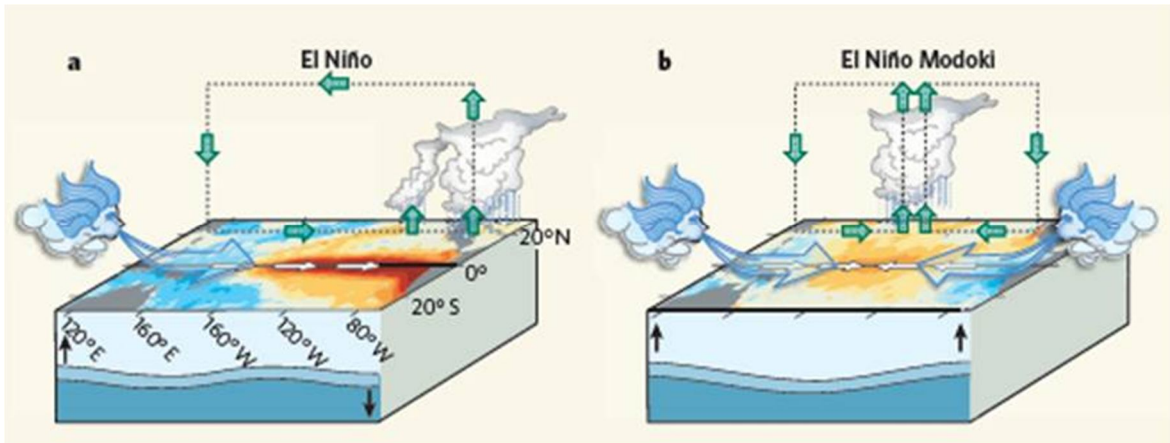


Figure 1.1 a) El Niño and b) El Niño Modoki conditions in tropical Pacific (Ashok and Yamagata, 2009).

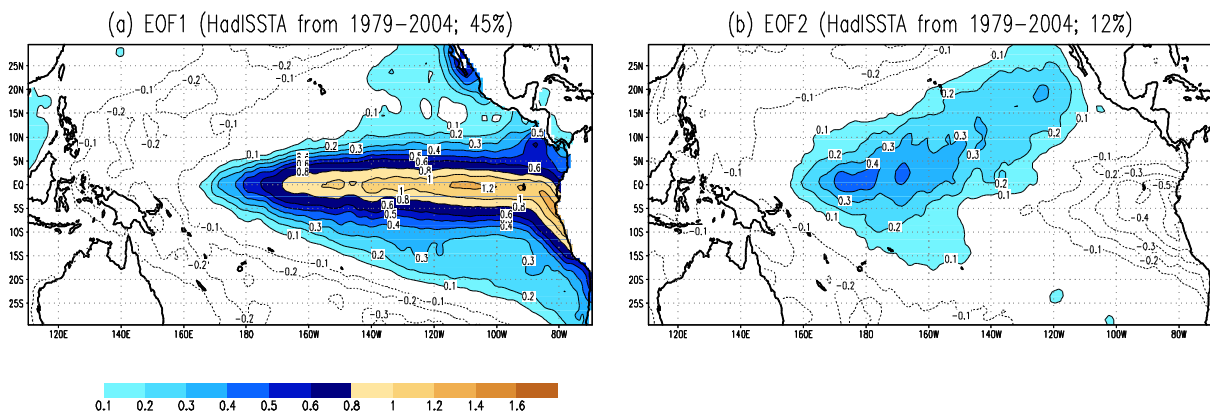


Figure 1.2 a) EOF1 mode b) EOF2 mode of tropical Pacific SSTA (1979–2004) (Ashok et al., 2007).

The leading mode of an empirical orthogonal function (EOF) analysis performed with Pacific Ocean SST yields the well-known El Niño pattern with peak SST anomalies in the eastern Pacific (Rasmusson and Carpenter, 1982; Trenberth, 1997). This mode accounts for approximately half the total variance of Pacific Ocean SST, depending on the dataset used and the period analyzed. For example, Ashok et al. (2007) obtained 45% of total variance in the El Niño mode (Fig. 1.2a) using the Hadley Centre Sea Ice and Sea Surface Temperature dataset (HadISST; Rayner et al. 2003) from the period 1979–2004. Recent studies have shown that the second mode of Pacific Ocean variability is represented by warm anomalies in SST located in the central Pacific, accounting for approximately 12% of total variance (Ashok et al. 2007;

Fig. 1.2b). The observed datasets are not long enough to have robust statistics for diagnostic studies. One possibility is to rely on many ocean–atmosphere Coupled General Circulation Model (CGCM) experiments to confirm the observational findings. The Intergovernmental Panel on Climate Change (IPCC) twentieth-century climate change model-phase 3 of the Coupled Model Intercomparison Project (CMIP3)-simulations (*Meehl et al., 2007*) are well suited for this purpose. For the fourth Assessment Report (AR4) of the IPCC, climate modeling groups have performed a well-coordinated set of twentieth century simulations (20C3M) and Special Report on Emissions Scenarios (SRES) A1B climate change experiments. For this purpose, climate modeling groups have used the state-of-the-art coupled ocean-atmosphere models.

The goals of this work are (1) to examine whether the IPCC climate models can reproduce El Niño and El Niño Modoki patterns as the fundamental statistical modes, as shown above (*Fig. 1.2*) by analysis of the AR4 datasets from the 20C3M and SRESA1B scenario; (2) evaluate the teleconnections between El Niño and El Niño Modoki with Indian Summer Monsoon Rainfall (ISMR) by regression analysis; (3) the future projections in SRESA1B are examined with Indian Summer Monsoon Rainfall (ISMR).

In this report, Data sets and statistical methodologies are described in Sect. 2, and then results are presented and discussed in Sect. 3. Finally, the main summary and conclusion are summarized in Sect. 4.

2. DATA AND METHODOLOGY

2.1) Datasets used

The following datasets are used in this study: (1) the global SST datasets from the Hadley Centre (*HadISST; Rayner et al., 2003*) to represent observations; (2) Gridded observational rainfall dataset for the Indian region (*Rajeevan et al., 2006*). The dataset is based on rainfall data of 1803 stations each with at least 90% data availability; (3) twentieth century simulations (20C3M) and Special Report on Emissions Scenarios (SRES) A1B scenario climate change run of SST and Precipitation performed by various modeling groups within the World Climate Research Programme's (WCRP's) Coupled Model Intercomparison Project phase 3 [CMIP3; see *Meehl et al. (2007)*; refer **Table 2.1** for a list of the models]. The control run is the twentieth-century climate change represented by the acronym simulations, carried out from 1901 to year 2000 with anthropogenic and natural forcing (20C3M). The climate change run corresponds to the climate change projection (that is, SRESA1B). The term 'SRESA1B' run refers to the last 100 years of the SRESA1B run, in which the concentration of CO₂ is fixed to about 700 p.p.m.

The time period considered in this study is boreal summer season (June-September; JJAS) and boreal winter season (December-February; DJF) for the last 30 years in the 20C3M and SRESA1B scenario. In this study the NINO3 index and the El Niño Modoki Index (EMI; *Ashok et al. (2007)*) are used. The definitions of the two indexes are as follows:

$$\text{Nino3} = [\text{SSTA}]_{\text{EP}},$$

where $[\text{SSTA}]_{\text{EP}}$ is the Sea Surface Temperature Anomalies (SSTA) averaged over the tropical Eastern Pacific (EP) (150°W to 90°W, 5°S to 5°N), and

$$\text{EMI} = [\text{SSTA}]_{\text{A}} - 0.5[\text{SSTA}]_{\text{B}} - 0.5[\text{SSTA}]_{\text{C}},$$

where $[\text{SST}]_{\text{A}}$, $[\text{SST}]_{\text{B}}$, and $[\text{SST}]_{\text{C}}$ stand for SSTA averaged over regions A (165°E to 140°W, 10°S to 10°N), B (110°W to 70°W, 15°S to 5°N), and C (125°E to 145°E, 10°S to 20°N), respectively.

2.2) CMIP3 dataset overview

In response to a proposed activity of the World Climate Research Programme's (WCRP's) Working Group on Coupled Modeling (WGCM), Program for Climate Diagnosis and Inter-comparison (PCMDI) volunteered to collect model output contributed by leading modeling centers around the world. Climate model output from simulations of the past, present and future climate was collected by PCMDI mostly during the years 2005 and 2006, and this archived data constitutes phase 3 of the Coupled Model Intercomparison Project (CMIP3). This collection of recent model output is officially known as the "**WCRP CMIP3 multi-model dataset**".

TABLE 2.1: Climate models available in WCRP CMIP3 dataset

Originating Group(s)	Country	CMIP3 I.D.	Abbreviation
Beijing Climate Center	China	BCC-CM1	bcc
Bjerknes Centre for Climate Research	Norway	BCCR-BCM2.0	bcr
Canadian Centre for Climate Modeling & Analysis	Canada	CGCM3.1(T47)	ccm
Canadian Centre for Climate Modeling & Analysis	Canada	CGCM3.1(T63)	ccm2
Météo-France / Centre National de Recherches Météorologiques	France	CNRM-CM3	cnr
CSIRO Atmospheric Research	Australia	CSIRO-Mk3.0	csr
CSIRO Atmospheric Research	Australia	CSIRO-Mk3.5	csr35
Max Planck Institute for Meteorology	Germany	ECHAM5/MPI-OM	ech
Meteorological Institute of the University of Bonn, Meteorological Research Institute of KMA, and Model and Data group.	Germany / Korea	ECHO-G	eco
US Dept. of Commerce / NOAA / Geophysical Fluid Dynamics Laboratory	USA	GFDL-CM2.0	gfo
US Dept. of Commerce / NOAA / Geophysical Fluid Dynamics Laboratory	USA	GFDL-CM2.1	gf1
NASA / Goddard Institute for Space Studies	USA	GISS-AOM	gao
NASA / Goddard Institute for Space Studies	USA	GISS-EH	gih
NASA / Goddard Institute for Space Studies	USA	GISS-ER	gir
Instituto Nazionale di Geofisicae Vulcanologia	Italy	INGV-SXG	ing
Institute for Numerical Mathematics	Russia	INM-CM3.0	inm

Institute Pierre Simon Laplace	France	IPSL-CM4	ips
Center for Climate System Research (The University of Tokyo), National Institute for Environmental Studies, and Frontier Research Center for Global Change (JAMSTEC)	Japan	MIROC3.2(hires)	mih
Center for Climate System Research (The University of Tokyo), National Institute for Environmental Studies, and Frontier Research Center for Global Change (JAMSTEC)	Japan	MIROC3.2 (medres)	mim
Meteorological Research Institute	Japan	MRI-CGCM2.3.2	mri
National Center for Atmospheric Research	USA	NCAT_PCM1	ncp
Hadley Centre for Climate Prediction and Research / Met Office	UK	UKMO-HadCM3	ukc
Hadley Centre for Climate Prediction and Research / Met Office	UK	UKMO-HadGEM1	ukg

2.3) METHODOLOGY

The analysis methods used in this study are Empirical Orthogonal Function (EOF), and correlation analysis. The methods are described briefly below:

A) Empirical Orthogonal Function

EOF technique aims at finding a new set of variables that capture most of the observed variance from the data through a linear combination of the original variables. EOFs have been introduced in atmospheric science by Lorenz (1956).

Suppose we have a long time series of data given by $X(x,y,t)$, such that its anomalies are given by

$$X(x, y, t) = X(x, y, t) - \overline{X(x, y, t)}^t$$

The goal of EOF analysis is to express the anomalies in terms of small number of EOFs $e_m(x,y)$, which represent spatial variability, with amplitudes $u_m(t)$ called principal components, i.e.

$$X(x, y, t) = \sum_{m=1}^M u_m(t) e_m(x, y)$$

The principal components, $u_m(t)$, tells us how the amplitude of each EOF varies with time. The EOF shows the spatial structure of the major factors that can account for the temporal variations of X .

The first EOF explains the greatest fraction of the total variance and the remaining empirical orthogonal functions account for the remaining variances. The construction of EOFs begin with the computation of the covariance matrix

$$R = X(x, y, t)^T X(x, y, s) = \begin{pmatrix} s_{11} & s_{12} & \dots & s_{1K} \\ s_{21} & s_{22} & \dots & s_{2K} \\ \dots & \dots & s_{ij} & \dots \\ s_{K1} & s_{K2} & \dots & s_{KK} \end{pmatrix}$$

where each element of the covariance matrix R is just the product of the anomalies at two different grid points. Then the covariance matrix averaged in time is given by

$$r_{ij} = \frac{1}{N} \sum_{t=1}^N X(x_i, y_i, t) X(x_j, y_j, t)$$

The covariance matrix, R , is a real symmetric matrix and therefore has eigenvectors, $e_m(x,y)$, and real, positive eigen values, λ_m , i.e.

$$R e_m = \lambda_m e_m$$

The eigenvectors, e_m , are the EOFs and are orthogonal, so they satisfy

$$\sum_{x,y=1}^N e_m(x_i, y_i) e_n(x_i, y_i) = 0, m \neq n$$

The principal components or time amplitudes are constructed by projecting the original data onto each EOF:

$$u_m(t) = \sum_{x,y=1}^N X(x,y,t)e_m(x,y)$$

B) Partial Correlation

Partial correlation technique (*Pedhazur, 1997; Spiegel, 1997; Ashok et al., 2001, 2003a, b; Saji and Yamagata, 2003*) is used to extract the teleconnections patterns. Partial correlation is a linear regression technique to isolate the influence of an independent predictor on a predictand by removing the association of the predictand with one or more other independent variables. The technique removes the masking impact of the other independent predictor. The partial correlation coefficient $r_{12.3}$ between two variables A1, A2, after removing the influence of the variable A3, is given by

$$r_{12.3} = \frac{r_{12} - r_{13} r_{23}}{\sqrt{(1 - r_{13}^2)(1 - r_{23}^2)}} \dots\dots\dots (A)$$

In equation (A) the term r_{ij} represents the linear correlation coefficient between A_i and A_j . The subscripts 1 and 2 refer to the two variable of interest, and the 3 refers to the variable whose influence is to be controlled.

3. RESULTS

3.1) Analysis of the 20C3M SST and comparison with observations for the period 1971-2000

An EOF analysis is performed on the boreal summer (JJAS) and winter (DJF) data from observations for the period 1971-2000. Similar analysis is also performed on the outputs from the 20C3M for the period of last thirty years SST anomalies to identify whether 23 coupled models from IPCC 20C3M dataset can reproduce ENSO and ENSO Modoki events.

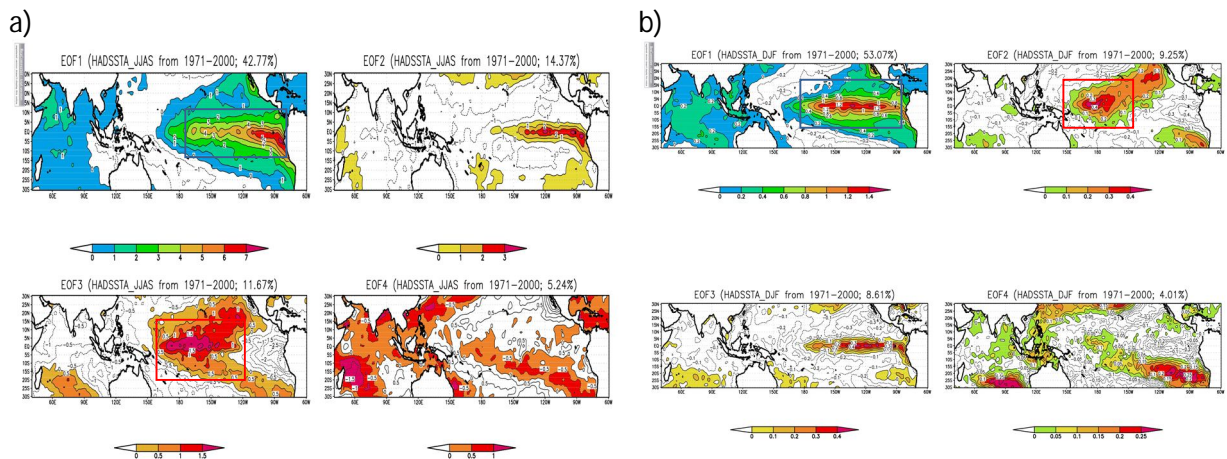


Figure 3.1 Top four EOF modes of SSTA **a)** JJAS **b)** DJF 1971-2000 from observation {Block indicates: Modoki (Red), El Niño (Blue)}.

The EOF1 pattern from observations (*Fig. 3.1a*) captures the well-known ENSO pattern (*Rasmusson and Carpenter, 1982*). This mode explains about 44.8% of the SST variance for the boreal summer season of the study period. The EOF2 explains 14.8% of the SST variability. The EOF3 that explains 11.5% of the SST variability captures a zonal tripole pattern in the tropical region (*Fig. 3.1a*). Both eastern and western tropical Pacific SSTAs have loadings of the same sign, while those of the central tropical Pacific are opposite. In higher latitudes, the positive loadings in the central equatorial Pacific spread eastward in both hemispheres. The EOF4 patterns explain only about 5.24% of the variance, respectively. The time series of the principal components (PCs) of EOF1, EOF2, EOF3 and EOF4 are presented in *Fig.*

1.1a. The correlation between PC1 and NINO3 index is very high, and amounts to 0.94, which proves that EOF1 represents the conventional El Niño well. The time series of the EMI is shown in Fig. 1.2a. The correlation between EMI and the PC3 is 0.91, which is statistically significant at a 99% confidence level. The EOF3 represents the ENSO Modoki for this period. During the boreal winter (DJF) EOF1 pattern from observations (Fig. 3.1b) captures the well-known ENSO pattern (Rasmusson and Carpenter, 1982). This mode explains about 53.07% of the SST variability for the study period. The EOF2 that explains 9.25% of the SST variability (Fig. 3.1b) has both eastern and western tropical Pacific SSTAs have loadings of the same sign, while those of the central tropical Pacific are opposite. In higher latitudes, the positive loadings in the central equatorial Pacific spread eastward in northern hemisphere. The negative loadings are observed in southern hemisphere. The EOF3 and EOF4 patterns explain only about 8.61% and 4.01% of the SST variance, respectively. The time series of the principal components (PCs) of EOF1, EOF2, EOF3 and EOF4 are presented in Fig 1.1b. The correlation between PC1 and NINO3 index is very high, and amounts to 0.96, which proves that EOF1 represents the conventional El Niño well. The time series of the EMI is shown in Fig 1.2b. The correlation between EMI and the PC2 is 0.73. The EOF2 represents the ENSO Modoki for this period.

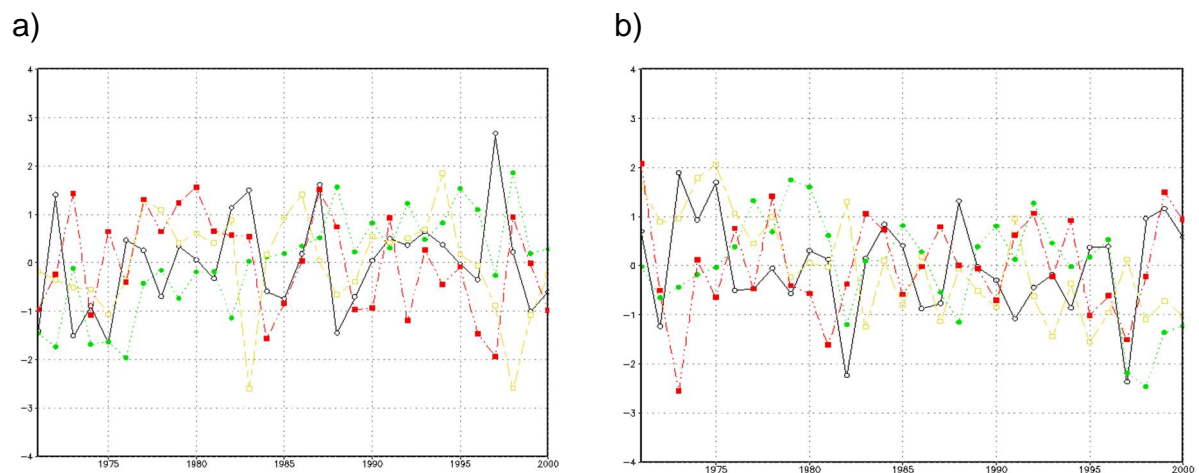


Figure 1.1 Time series of PC1 (solid black), PC2 (dotted green), PC3 (long dash, short dash yellow), PC4 (dot dot dash red) (a) JJAS (b) DJF in the HadISST (observations) for the period 1971-2000.

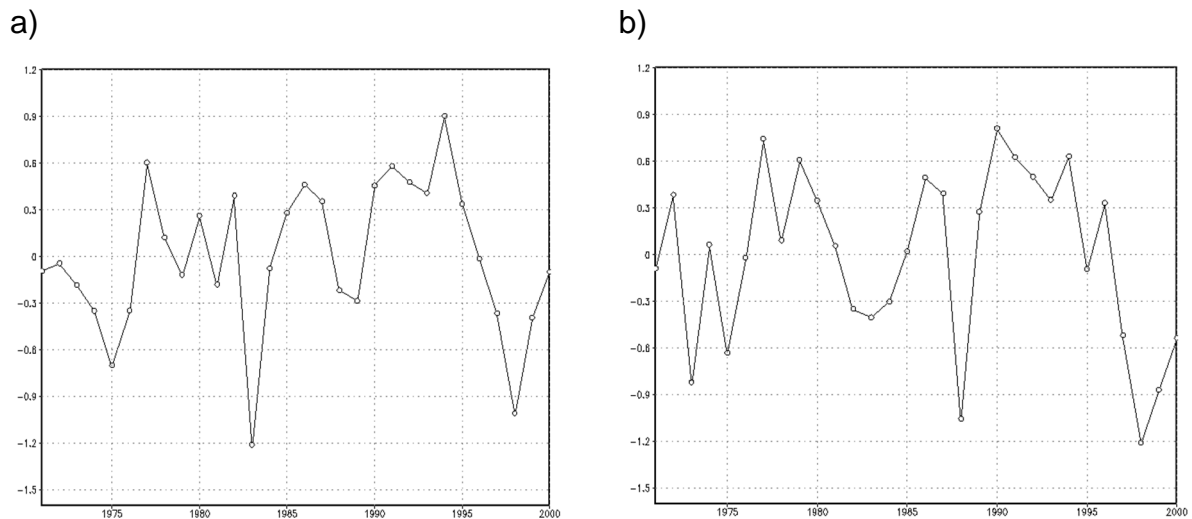
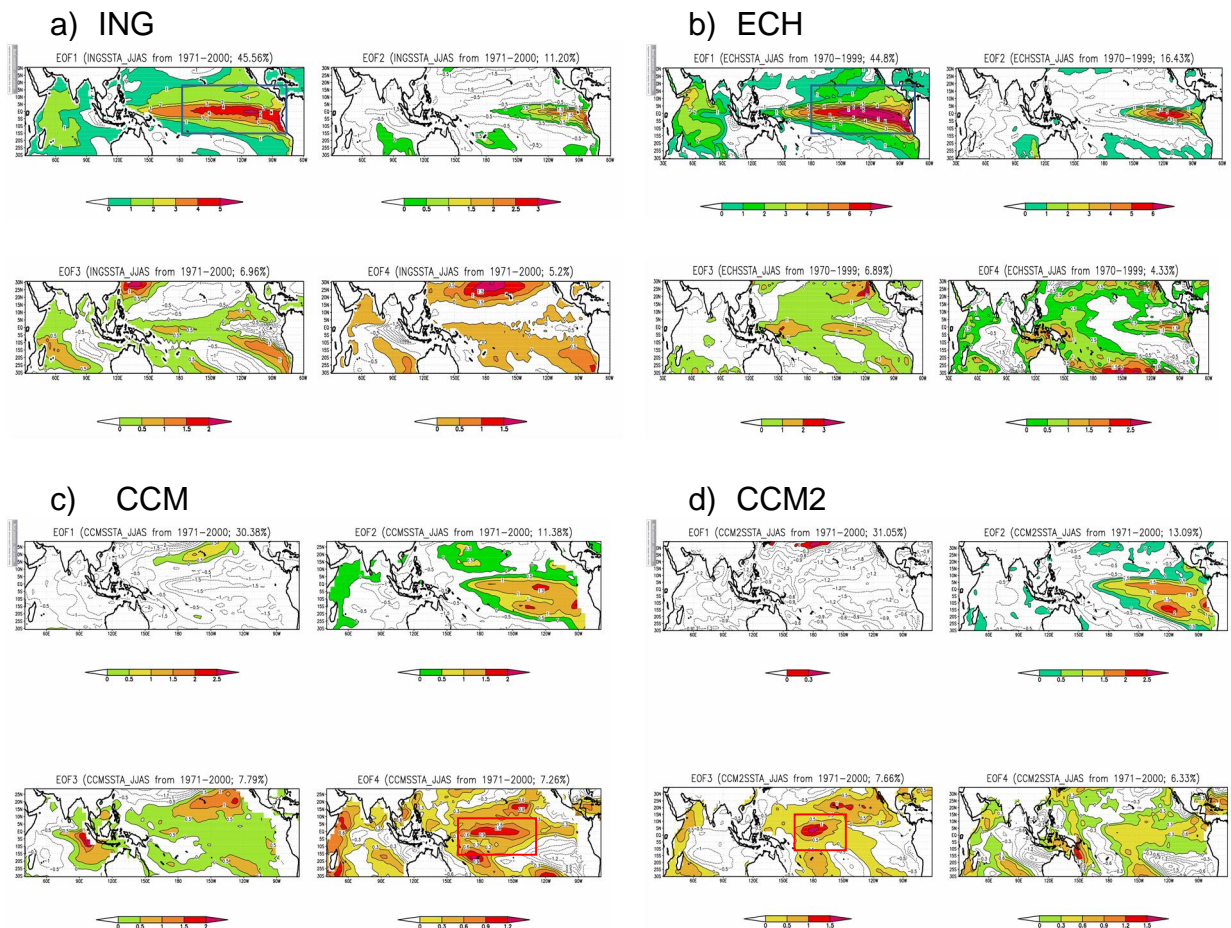


Figure 1.2 Time series of ENSO Modoki index (a) JJAS (standard deviation of the EMI is 0.47°C) (b) DJF (standard deviation of the EMI is 0.55°C) in the HadISST (observations) for the period 1971-2000.

Only 25% of the models from 20C3M capture the ENSO and ENSO Modoki pattern similar to the observations (*Fig. 3.1*) to some extent in JJAS (*Fig. 3.2; Table 2.1*) and DJF (*Fig. 3.3; Table 2.2*). Even in most of this more realistic model, the latitudinal width of these captured modes differs from that of the observations. For the JJAS season only 2 out of the 23 models, namely ING and ECH (*Fig. 3.2a, b*), capture ENSO. The CCM and CCM2 (*Fig. 3.2c, d*) models are able to capture ENSO Modoki. Only two models GFO and GF1 (*Fig. 3.2e, f*) simulates both ENSO and ENSO Modoki as important modes. The remaining models (*Table 2.1*) are not able to reproduce ENSO and ENSO Modoki patterns in JJAS for the study period.

Table 2.1 Categorization of simulated ENSO flavors in 20C3M for boreal summer season (JJAS). (* represents ENSO and # represents ENSO Modoki in corresponding mode of EOF).

Models in 20C3M (JJAS)	EOF modes and corresponding variance explained (%)			
	EOF 1	EOF 2	EOF 3	EOF 4
ING	45.56*	11.20	6.96	5.20
ECH	44.80*	16.43	6.89	4.33
CCM	30.38	11.38	7.79	7.26#
CCM2	31.05	13.09	7.66#	6.33
GFO	47.08*	16.32	6.56	5.80#
GF1	61.87*	15.04#	4.91	3.82



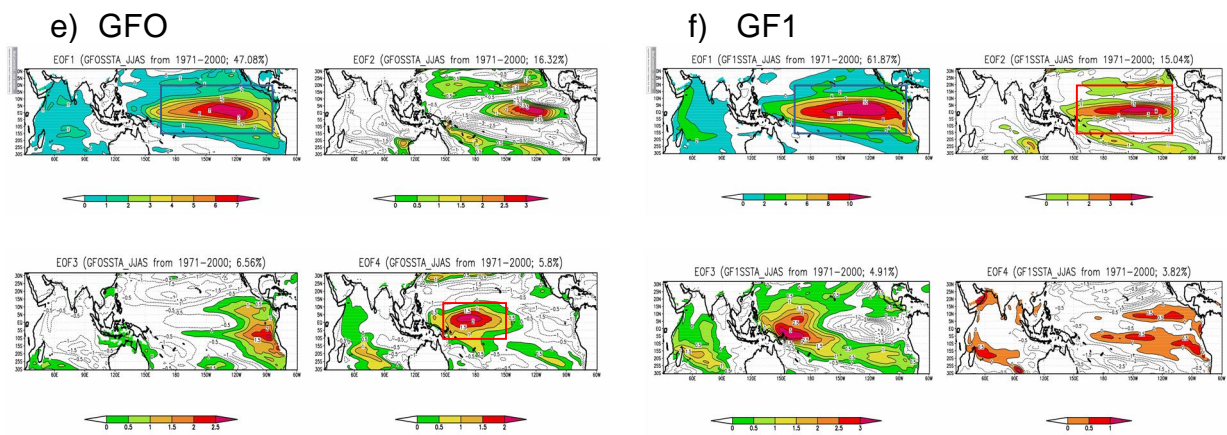


Figure 3.2 Above first four EOF modes of SSTA-JJAS (20C3M) for the models listed in Table 2.1 {Block indicates: Modoki (Red), El Niño (Blue)}.

The ING and ECH models capture the ENSO pattern (*Fig. 3.2a and b*) a leading mode with a variance of 45.56% and 44.80% in JJAS 20C3M. The ENSO pattern is extended towards westward of equatorial tropical Pacific and positive loadings spread in northern hemisphere and in the eastern equatorial Pacific spread southward in southern hemispheres in both the models. The correlation between PC1 and NINO3 index is 0.95 for ING, which is statistically significant at a 99% confidence level. The correlation between PC1 and NINO3 index for ECH is 0.38. The EOF2 pattern in the ING (ECH) model explains only about 11.20% (16.43%) of the SST variance. The EOF3 and EOF4 patterns explain only about 6.96% (5.20%) and 6.89% (4.33%) of the SST variance for the ING (ECH) model, respectively. The ENSO Modoki pattern is captured by CCM (*Fig. 3.2c*) and CCM2 (*Fig. 3.2d*) in EOF4 and EOF3 modes respectively with a variance of 7.26% and 7.66%. In EOF4 of CCM (*Fig. 3.2c*) positive loadings are spread eastward of tropical Pacific in higher altitudes of northern hemisphere and westward of tropical Pacific of southern hemisphere. In EOF3 of CCM2 (*Fig. 3.2d*) in higher latitudes, the positive loadings in the central equatorial Pacific spread eastward in northern hemisphere and southward in southern hemisphere. The EOF1, EOF2 and EOF3 pattern of CCM (*Fig. 3.2c*) explains about 30.40%, 11.40% and 7.79% of the SST variance. The EOF1, EOF2 and EOF4 pattern of CCM (*Fig. 3.2d*) explains about 31.05%, 13.09% and 6.33% of the SST variance, respectively. The correlation between PC4 and EMI is 0.75 for CCM and for

CCM2 correlation between PC3 and EMI is 0.84. The ENSO and ENSO Modoki pattern both are captured by the models GFO and GF1 in JJAS 20C3M. The EOF1 pattern of GFO (*Fig. 3.2e*) captures the well-known ENSO pattern (*Rasmusson and Carpenter, 1982*). This mode explains about 47.08% of the SST variance. The ENSO pattern is extended towards westward of equatorial tropical Pacific and positive loadings spread in northern hemisphere (*Fig. 3.2e*). The EOF2 and EOF3 explain 16.32% and 6.56% of the SST variance, respectively. The EOF4 that explains 5.8% (*Fig. 3.2e*) of the SST variance captures a pattern similar to ENSO Modoki in the central tropical Pacific region but its latitudinal widths are slightly different than the observations (*Fig. 3.1a*). The correlation for the model GFO between PC1 and NINO3 index is 0.97. The correlation is very high, which proves that EOF1 represents the conventional El Niño well in GFO. The correlation for the model GFO between PC4 and EMI is 0.60. The EOF1 pattern of GF1 (*Fig. 3.2f*) captures the well-known ENSO pattern (*Rasmusson and Carpenter, 1982*). This mode explains about 61.87% of the SST variance. The ENSO pattern is extended towards westward of equatorial tropical Pacific and positive loadings spread eastward in both hemisphere (*Fig. 3.2f*). The EOF2 that explains 15.04 % (*Fig. 3.2f*) of the SST variance captures a pattern similar to ENSO Modoki in the central tropical Pacific with positive (negative) loadings in the northern (southern) hemisphere. The EOF2 and EOF3 explain 4.91% and 3.82% of the SST variance (*Fig. 3.2f*), respectively. The correlation for the model GF1 between PC1 and NINO3 index is 0.98. The correlation is very high, which proves that EOF1 represents the conventional ENSO well in GF1. The correlation for the model GF1 between PC2 and EMI is 0.64. The remaining models (Table 2.1) fail to reproduce ENSO and ENSO Modoki pattern in JJAS 20C3M for the study period. The time series of the principal components (PCs) of EOF1, EOF2, EOF3 and EOF4 for the models *ING, ECH, CCM, CCM2, GFO and GF1* in JJAS 20C3M are presented in *Fig. 2.1* and EMI for the models *CCM, CCM2, GFO and GF1* in JJAS 20C3M are presented in *Fig. 2.2*.

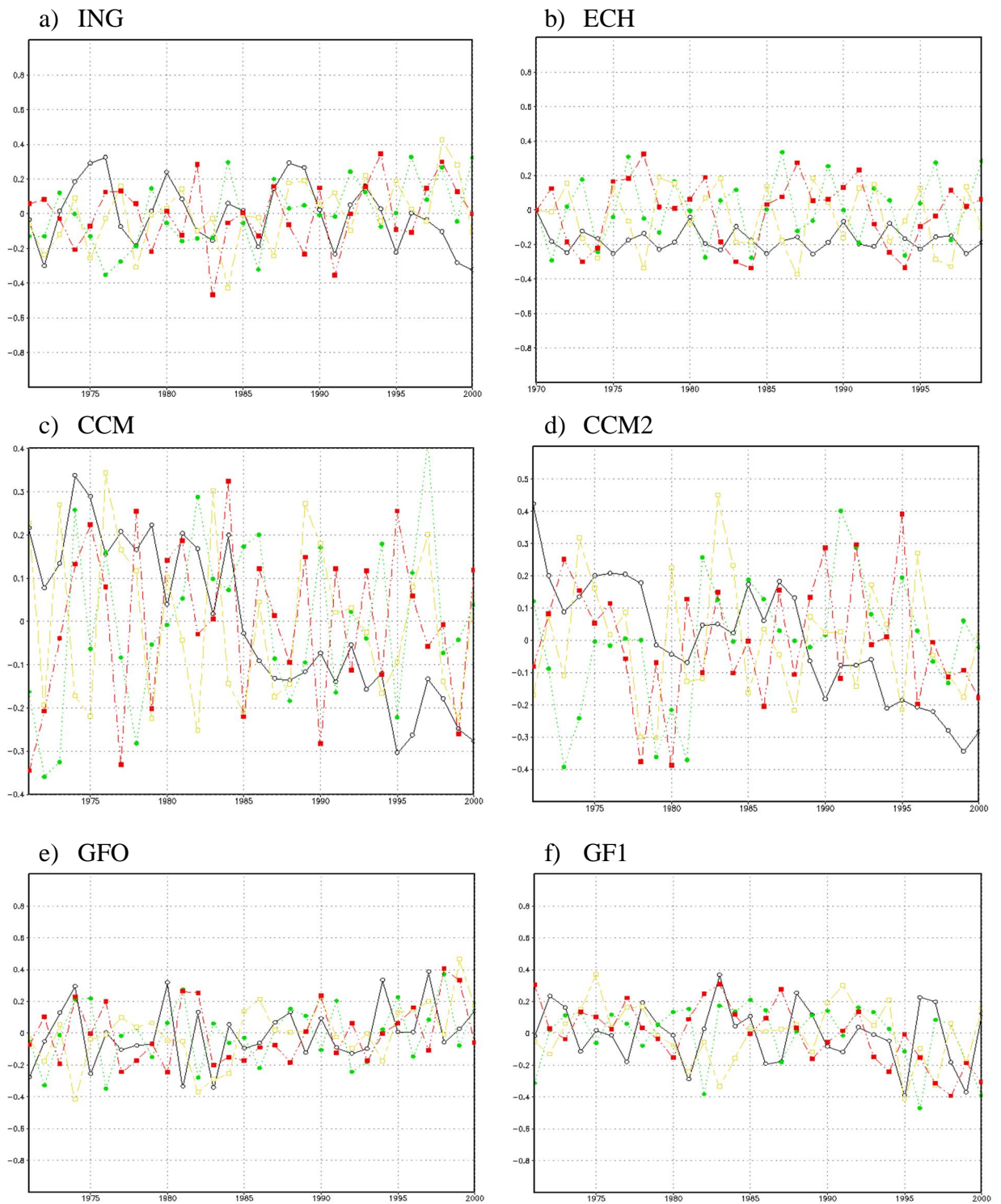
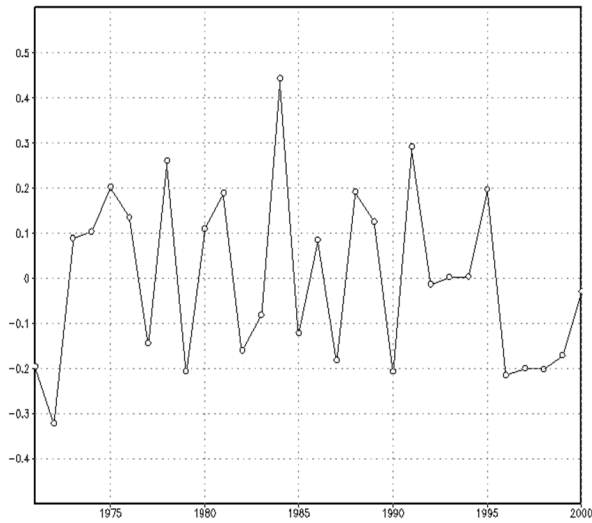
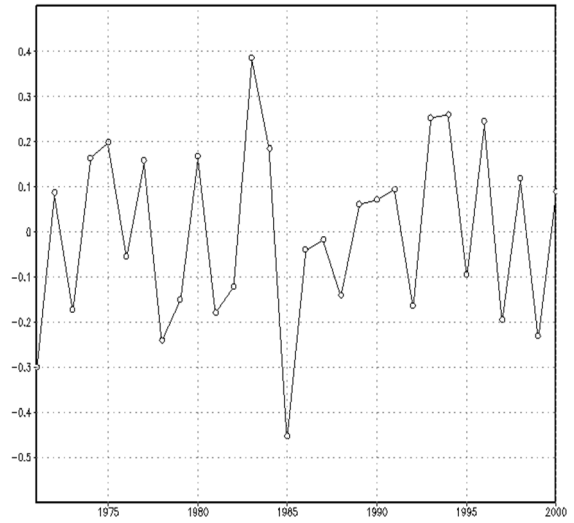


Figure 2.1 Time series of PC1 (solid black), PC2 (dotted green), PC3 (long dash, short dash yellow), PC4 (dot dot dash red) for the models in JJAS 20C3M (a) ING (b) ECH (c) CCM (d) CCM2 (e) GFO (f) GF1.

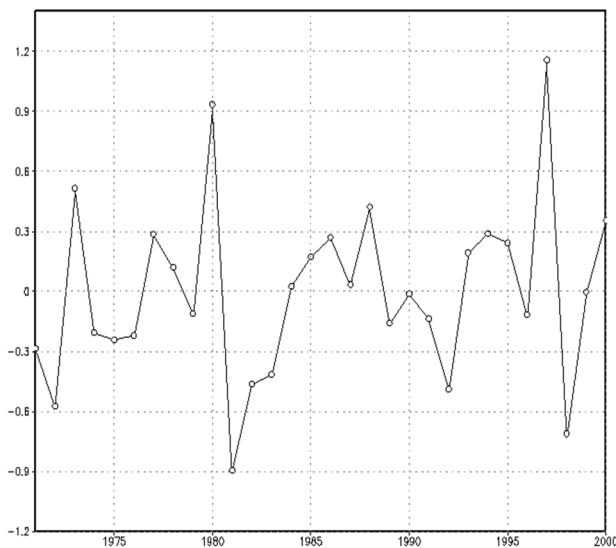
a) CCM



b) CCM2



c) GFO



d) GF1

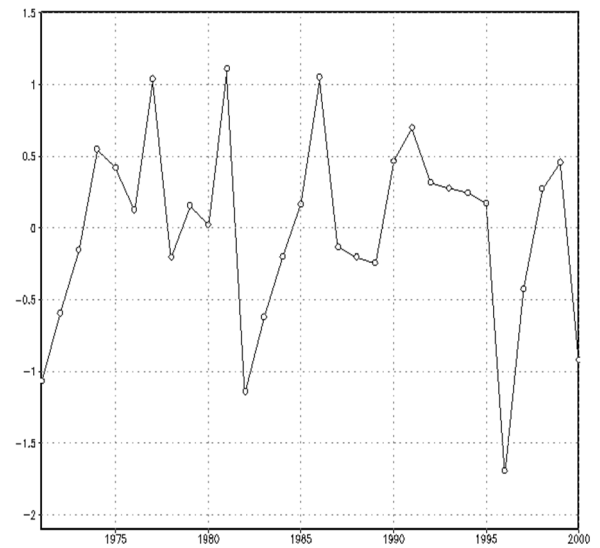


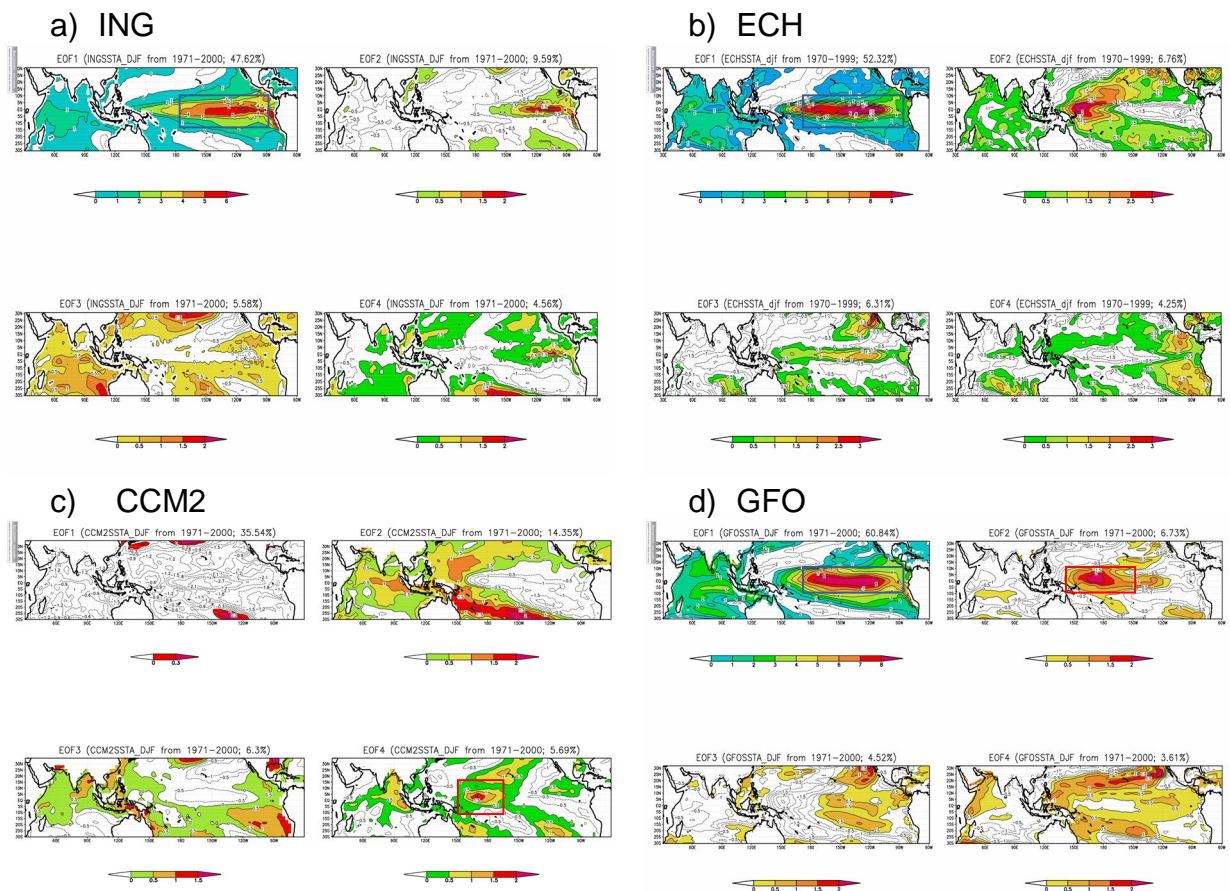
Figure 2.2 Time series of ENSO Modoki index (*standard deviation*) (a) CCM (0.19°C) (b) CCM2 (0.19°C) (c) GFO (0.44°C) (d) GF1 (0.65°C) for JJAS in 20C3M.

Similarly in DJF for the same time period as of JJAS 20C3M very few of the models capture an ENSO and ENSO Modoki. The ING, ECH and GF1 (*Fig. 3.3a, b and e*) models capture the ENSO pattern a leading mode with a variance of 45.56% and 44.80%. The ENSO pattern is extended towards westward of equatorial tropical Pacific. The EOF2, EOF3 and EOF4 explain the variance of 9.59%, 5.58% and 4.56% (ING; *Fig. 3.3a*), 6.76%, 6.31% and 4.25% (ECH; *Fig. 3.3b*) and 24.17%,

6.24% and 3.75% (GF1; *Fig. 3.3e*). The correlation between PC1 and NINO3 index for the models ING, ECH and GF1 is 0.96, 0.97 and 0.97 is statistically significant at a 99% confidence level, which proves that EOF1 represents the conventional El Niño well. The ENSO Modoki pattern is captured by the model CCM2 (*Fig. 3.3c*). The EOF1, EOF2 and EOF3 explain the variance of 35.54%, 14.35% and 6.30% of the variance, respectively. EOF4 mode captures the ENSO Modoki pattern with a variance of 5.69% with positive loadings spread in northern hemisphere and in southern hemisphere of tropical Pacific. The correlation between PC4 and EMI is 0.51 for CCM2. The ENSO and ENSO Modoki pattern both are captured by the model GFO in DJF 20C3M. The EOF1 pattern of GFO (*Fig. 3.3d*) captures El Niño pattern (*Rasmusson and Carpenter, 1982*). This mode explains about 60.84% of the SST variance. The EOF2 mode explains 6.73% of the SST variance with anomalous SSTA in the central tropical Pacific and spread eastward of equatorial tropical Pacific and negative loadings spread at higher latitudes in both the hemispheres (*Fig. 3.3d*). The EOF3 and EOF4 explain 4.52% and 3.61% of the SST variance, respectively. The correlation of GFO between PC1 and NINO3 index is 0.98. The correlation is very high, which proves that EOF1 represents the conventional ENSO well in GFO. The correlation of GFO between PC2 and EMI is 0.51. The time series of the principal components (PCs) of EOF1, EOF2, EOF3 and EOF4 for the models *ING, ECH, CCM2, GFO and, GF1* in DJF 20C3M are presented in *Fig. 3.1* and EMI for the models *CCM2 and GFO* in DJF 20C3M are presented in *Fig. 3.2*. The model CCM and GF1 fails to reproduce the ENSO Modoki pattern in DJF as of JJAS for the study period. The remaining models are not able to reproduce ENSO and ENSO Modoki patterns in DJF for the study period.

Table 2.2 Categorization of simulated ENSO flavors in 20C3M for boreal winter season (DJF). (* represents ENSO and # represents ENSO Modoki in corresponding mode of EOF).

Models in 20C3M (DJF)	EOF modes and corresponding variance explained (%)			
	EOF 1	EOF 2	EOF 3	EOF 4
ING	47.62*	9.59	5.58	4.56
ECH	52.32*	6.76	6.31	4.25
CCM2	35.54	14.35	6.30	5.69#
GFO	60.84*	6.73#	4.52	3.61
GF1	51.90*	24.17	6.24	3.75



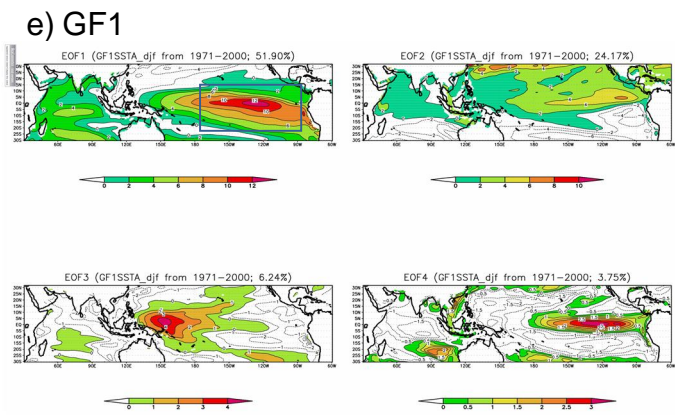
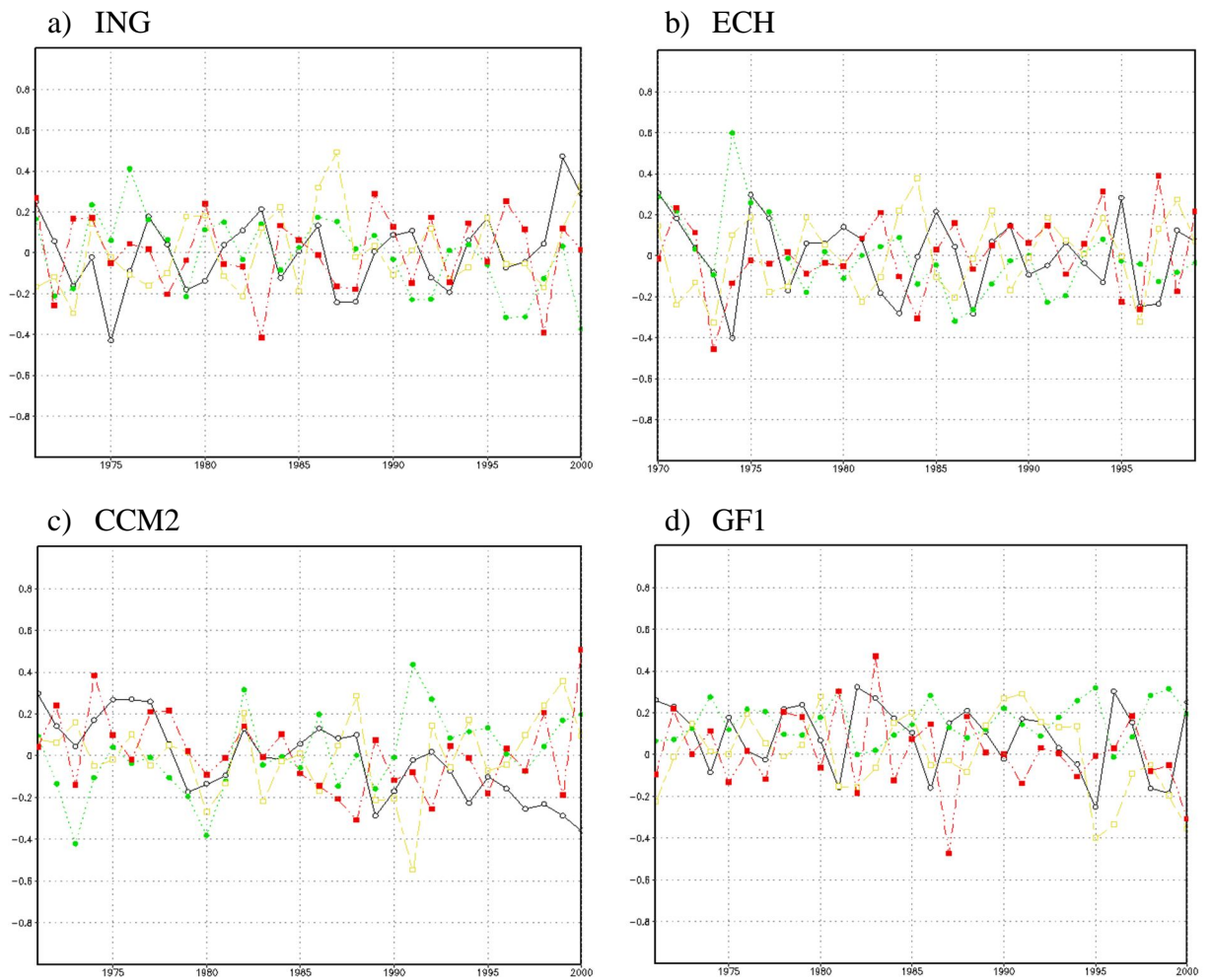


Figure 3.3 Above first four EOF modes of SSTA-DJF (20C3M) for the models listed in Table 2.2 {Block indicates: Modoki (Red), El Niño (Blue)}.



e) GFO

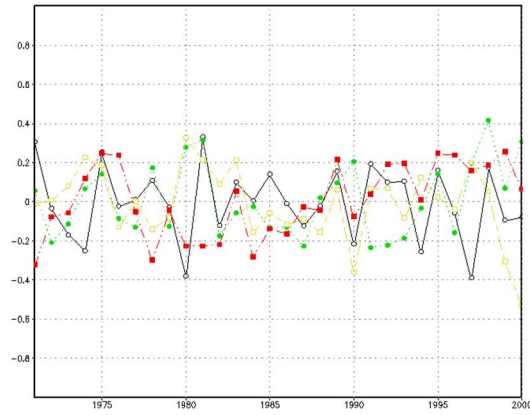
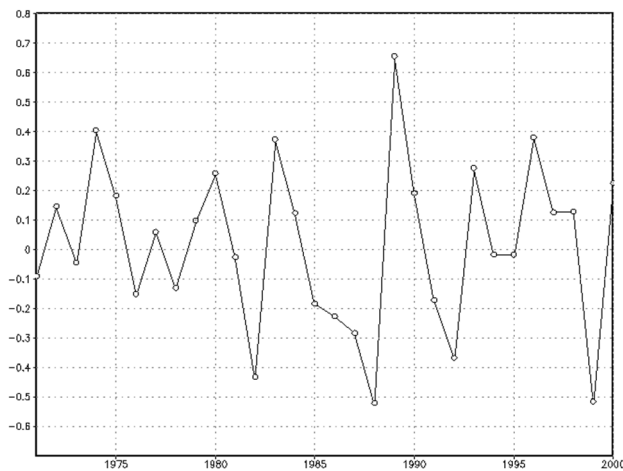


Figure 3.1 Time series of PC1 (solid black), PC2 (dotted green), PC3 (long dash, short dash yellow), PC4 (dot dot dash red) for the models in DJF 20C3M (a) ING (b) ECH (c) CCM2 (d) GF1 (e) GFO.

a) CCM2



b) GFO

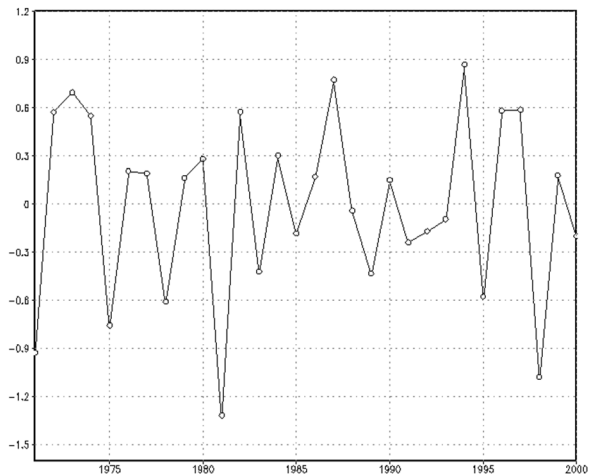


Figure 3.2 Time series of ENSO Modoki index (*standard deviation*) (a) CCM2 (0.23°C) (b) GFO (0.57°C) for DJF in 20C3M.

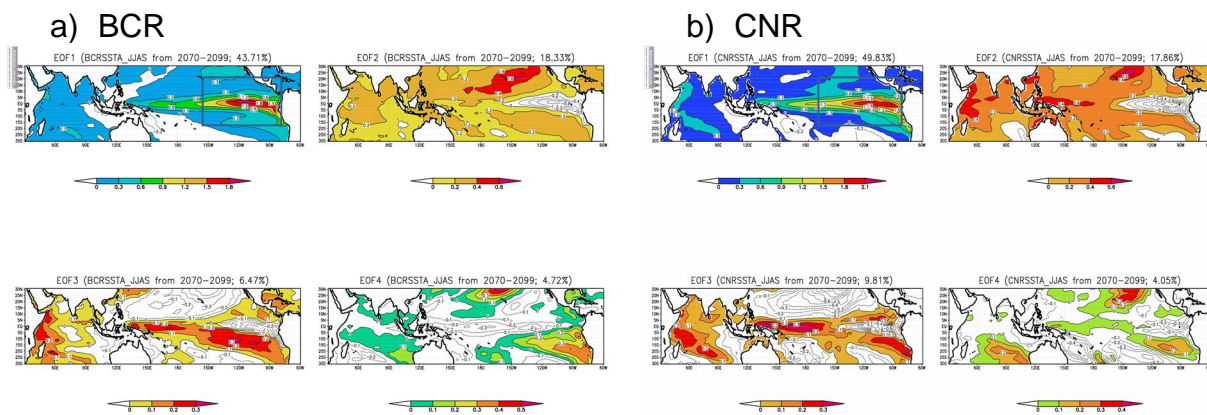
3.2) Models simulations in SRESA1B scenario

Only 20% of the models from SRESA1B capture the ENSO or ENSO Modoki pattern similar to the observations (*Fig. 3.1*) to some extent in JJAS (*Fig. 3.4*; *Table*

3.1) and DJF (Fig. 3.5; Table 3.2). Even in most of this more realistic model, the latitudinal width of these captured modes differs from that of the observations. For the JJAS season only 2 out of the 23 models, namely BCR and CNR (Fig. 3.4a, b), capture ENSO. The model ECO (Fig. 3.4c) is able to capture ENSO Modoki and three models ECH, GFO and GF1 (Fig. 3.4d, e and f) simulates both ENSO and ENSO Modoki as important modes. The remaining models are not able to reproduce ENSO and ENSO Modoki patterns in JJAS for the study period.

Table 3.1 Categorization of simulated ENSO flavors in SRESA1B for boreal summer season (JJAS). (* represents ENSO and # represents ENSO Modoki in corresponding mode of EOF).

Models in SRESA1B (JJAS)	EOF modes and corresponding variance explained (%)			
	EOF 1	EOF 2	EOF 3	EOF 4
BCR	43.71*	18.33	6.47	4.72
CNR	49.83*	17.86	9.81	4.05
ECO	33.72	15.89	8.67 [#]	5.42
GFO	59.23*	11.86 [#]	5.26	3.24
GF1	58.70*	8.77 [#]	7.32	3.54
ECH	39.33*	14.17 [#]	12.69	6.01



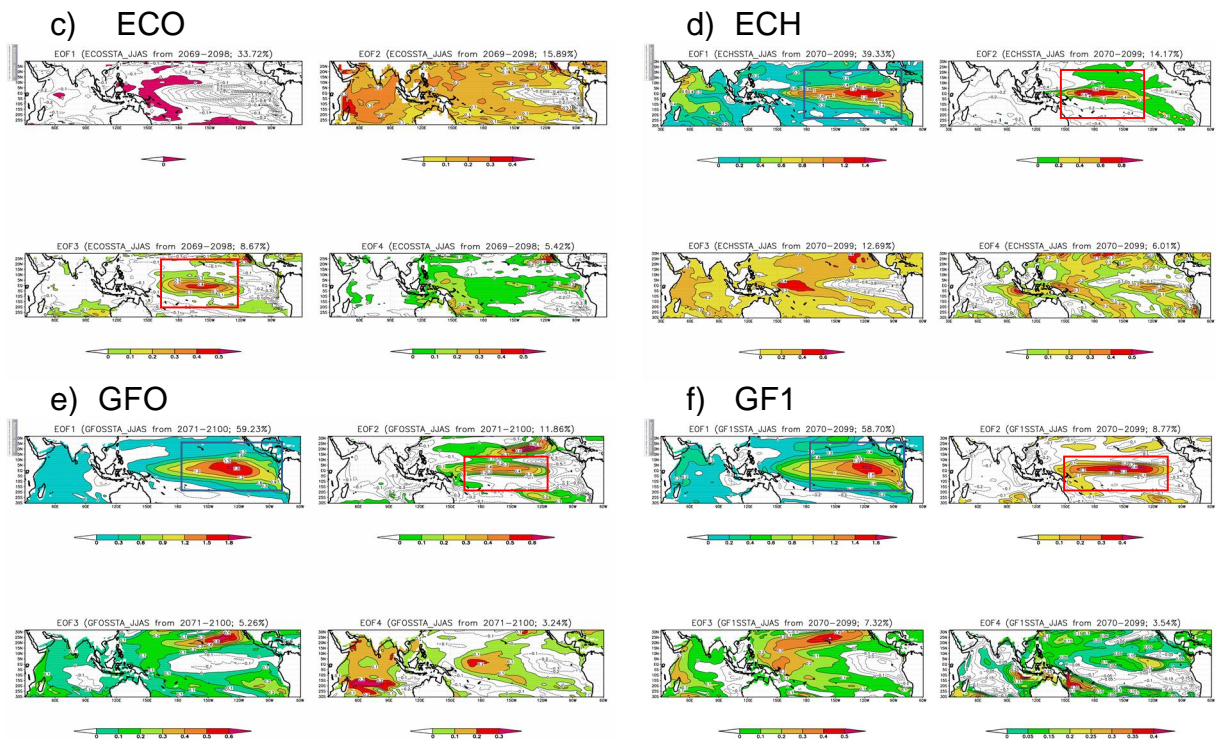
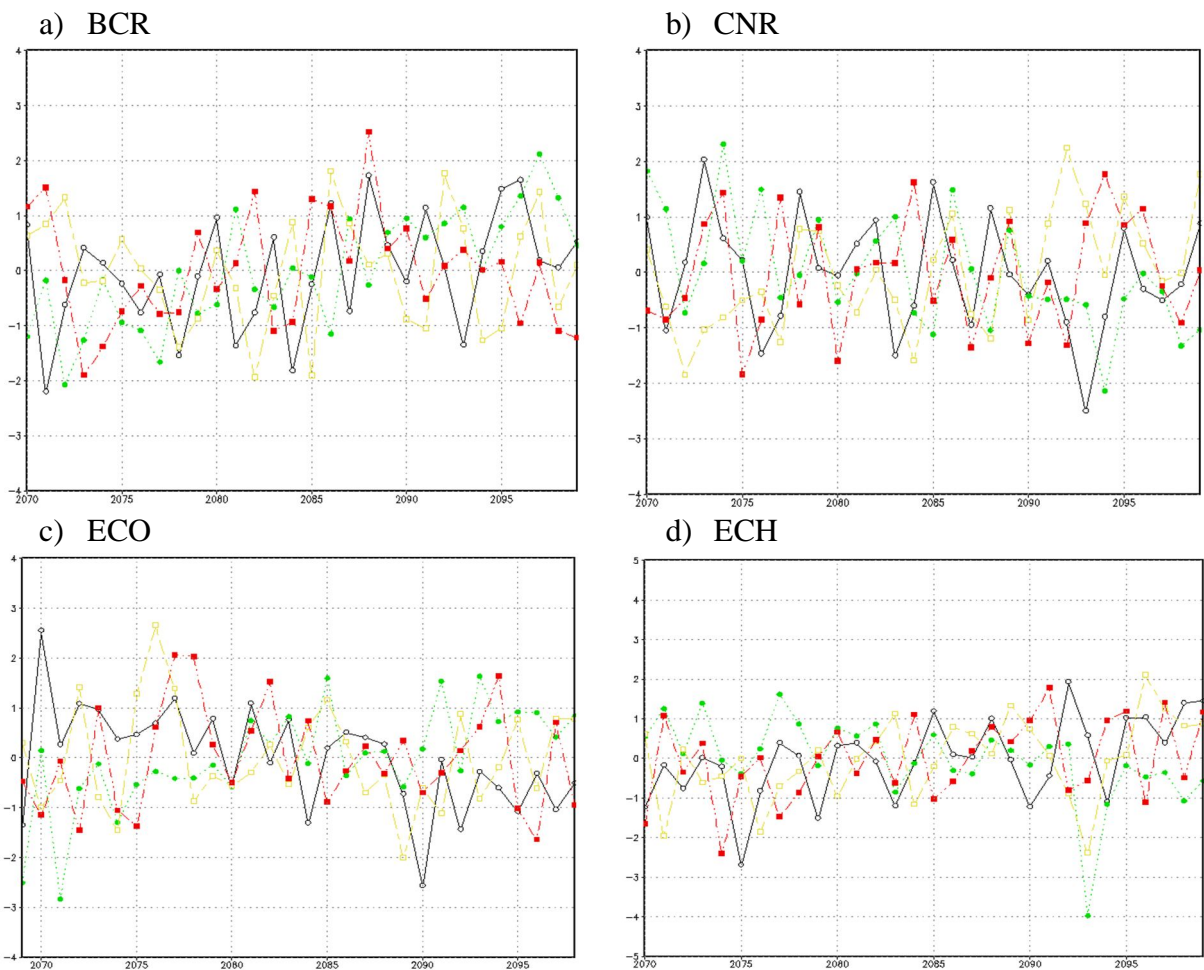


Figure 3.4 Top four EOF modes of SSTA-JJAS (SRESA1B) for the models listed in Table 3.1 {Block indicates: Modoki (Red), El Niño (Blue)}.

The BCR and CNR models capture the ENSO pattern (*Fig. 3.4a and b*) a leading mode with a variance of 43.71% and 49.83% in JJAS of SRESA1B. ENSO pattern is extended towards westward of equatorial tropical Pacific. Positive loadings spread in northern hemisphere, southeast of tropical Pacific and negative loadings spread in the southwest of tropical Pacific in both the models. The EOF2, EOF3 and EOF4 pattern of the model BCR (CNR) as shown in *Fig. 3.4a* (*Fig. 3.4b*) explains about 18.33% (17.86%), 6.47% (9.81%) and 4.72% (4.05%) of the SST variance, respectively. The correlation between PC1 and NINO3 index for the model BCR and CNR is 0.95 and 0.94, which is statistically significant at a 99% confidence level. The correlation is very high, which proves that EOF1 represents the conventional ENSO well in BCR and CNR. The ENSO Modoki pattern is captured by ECO (*Fig. 3.4c*). The EOF1 and EOF2 pattern of ECO (*Fig. 3.4c*) explains about 33.72% and 15.89% of the SST variance. The ENSO Modoki pattern is captured by ECO (*Fig. 3.4c*) in EOF3 mode with a variance of 8.67%. In EOF3 of ECO (*Fig. 3.4c*) both eastern and western

tropical Pacific SSTAs have loadings of the same sign, while those of the central tropical Pacific are opposite. In higher latitudes, the negative loadings are spread westward and the positive loadings are spread eastward in both hemispheres. The EOF4 pattern of ECO (*Fig. 3.4c*) explains about 5.42% of the SST variance, respectively. The correlation between PC3 and EMI is 0.80 for the model ECO. The EOF3 shows the ENSO Modoki for that period in the model ECO. The ENSO and ENSO Modoki pattern both are captured by the models GFO, GF1 and ECH in JJAS of SRESA1B. The EOF1 pattern of GFO (*Fig. 3.4e*) captures the well-known ENSO pattern (*Rasmusson and Carpenter, 1982*). This mode explains about 59.23% of the SST variance. The ENSO pattern is extended towards westward of equatorial tropical Pacific and positive loadings are spread in northern hemisphere (*Fig. 3.4e*). The EOF2 that explains 11.86% (*Fig. 3.4e*) of the SST variance captures a pattern similar to ENSO Modoki in the central tropical Pacific region but its latitudinal widths are slightly different than the observations (*Fig. 3.1a*) and positive loadings are seen in higher latitudes of northern hemisphere. The EOF3 and EOF4 explain 5.26% and 3.24% of the SST variance, respectively. The correlation for the model GFO between PC1 and NINO3 index is 0.99. The correlation is very high, which proves that EOF1 represents the conventional El Niño well in GFO. The correlation for the model GFO between PC2 and EMI is 0.67. The EOF1 pattern of GF1 (*Fig. 3.4f*) captures the well-known ENSO pattern (*Rasmusson and Carpenter, 1982*). This mode explains about 58.70% of the SST variance. The ENSO pattern is extended towards westward of equatorial tropical Pacific and negative loadings are spread in both hemisphere (*Fig. 3.4f*). The EOF2 that explains 8.77% (*Fig. 3.4f*) of the SST variance captures a pattern similar to ENSO Modoki in the central tropical Pacific region and negative loadings are seen in both the hemisphere. The EOF3 and EOF4 explain 7.32% and 3.54% of the SST variance, respectively. The correlation for the model GF1 between PC1 and NINO3 index is 0.98. The correlation is very high, which proves that EOF1 represents the conventional ENSO well in GF1. The correlation for the model GF1 between PC2 and EMI is 0.56. The EOF1 pattern of ECH (*Fig. 3.4d*) captures the well-known ENSO pattern (*Rasmusson and Carpenter, 1982*). This mode explains about 39.33% of the SST variance. The positive loadings spread in both hemispheres (*Fig. 3.4d*). The EOF2 that explains 14.17% (*Fig. 3.4d*) of the SST variance captures

an ENSO Modoki pattern in the central tropical Pacific. In higher latitudes, the positive loadings in the central equatorial Pacific spread eastward in both hemispheres. The EOF3 and EOF4 explain 12.69% and 6.01% of the SST variance (*Fig. 3.4d*), respectively. The correlation for the model ECH between PC1 and NINO3 index is 0.89. The correlation for the model ECH between PC2 and EMI is 0.74. The remaining models fail to reproduce ENSO and ENSO Modoki pattern in JJAS of SRESA1B for the study period. The time series of the principal components (PCs) of EOF1, EOF2, EOF3 and EOF4 for the models *BCR*, *CNR*, *ECO*, *ECH*, *GFO* and *GF1* in JJAS SRESA1B are presented in Fig.4.1 and EMI for the models *ECO*, *ECH*, *GFO* and *GF1* in JJAS SRESA1B are presented in Fig.4.2.



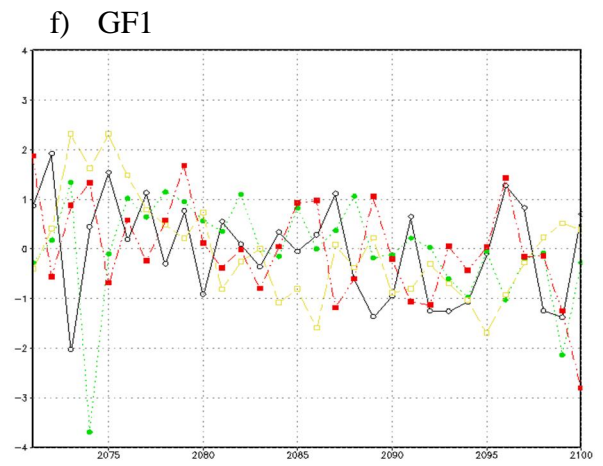
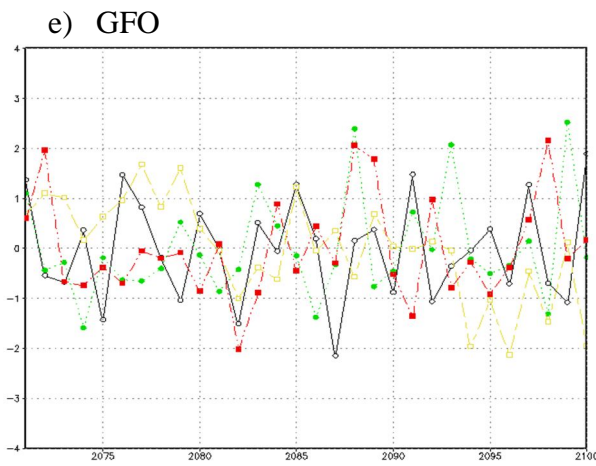
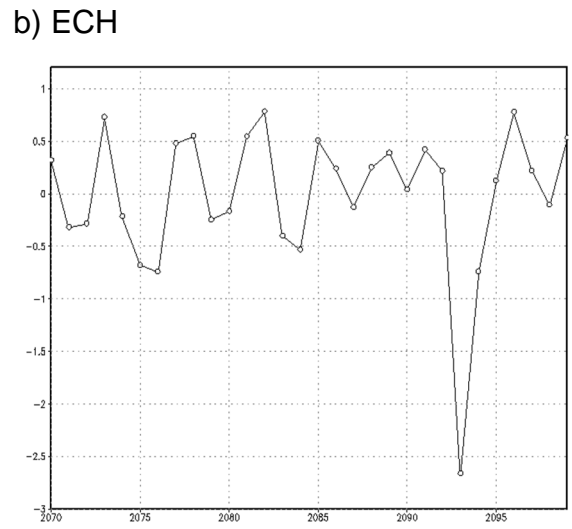
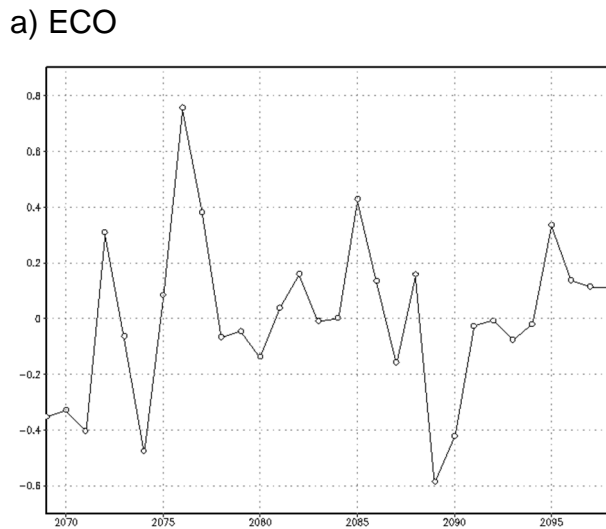
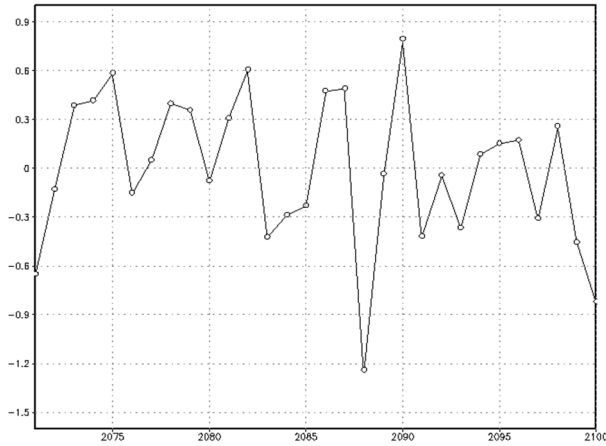


Figure 4.1 Time series of PC1 (solid black), PC2 (dotted green), PC3 (long dash, short dash yellow), PC4 (dot dot dash red) for the models in JJAS SRESA1B (a) BCR (b) CNR (c) ECO (d) ECH (e) GFO (f) GF1.



c) GFO



d) GF1

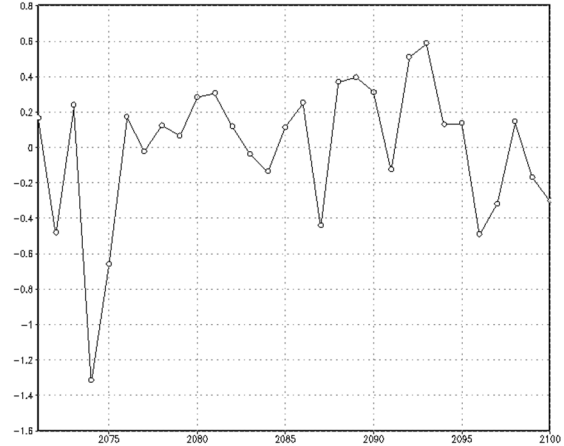


Figure 4.2 Time series of ENSO Modoki index (*standard deviation*) (a) ECO (0.28°C) (b) ECH (0.67°C) (c) GFO (0.46°C) (d) GF1 (0.39°C) for JJAS in SRESA1B.

Similarly in DJF for the same time period as of JJAS SRESA1B very few of the models capture an ENSO and ENSO Modoki. The BCR, CNR, GFO and GF1 (*Fig. 3.5a, b, d and e*) models capture the El Niño pattern a leading mode with a variance of 48.62%, 59.98%, 52.10% and 51.70%, respectively. The EOF2, EOF3 and EOF4 explain the variance of 10.90%, 6.23% and 5.26% for the model BCR. The EOF2, EOF3 and EOF4 explain the variance of 10.89%, 6.89% and 3.84% for the model CNR. The EOF2, EOF3 and EOF4 explain the variance of 7.34%, 5.07% and 4.68% for the model GFO. The EOF2, EOF3 and EOF4 explain the variance of 11.26%, 6.02% and 4.08% for the model GF1%, respectively. The correlation between PC1 and NINO3 index for the models BCR, CNR, GFO, and GF1 is 0.98, 0.98, 0.97 and 0.94, respectively. The correlation is very high, which proves that EOF1 represents the conventional ENSO well in these models. The ENSO and ENSO Modoki pattern both are captured by the model ECH in DJF of SRESA1B. The EOF1 pattern of ECH (*Fig. 3.5c*) captures ENSO pattern (*Rasmusson and Carpenter, 1982*). This mode explains about 50.47% of the SST variance. The EOF2 mode explains 10.31% of the SST variance. Both eastern and western tropical Pacific SSTAs have loadings of the same sign, while those of the central tropical Pacific are opposite. In higher latitudes, the negative loadings are spread in both hemispheres. The EOF2 shows the ENSO Modoki in this model for the study period. The EOF3 and EOF4 explain 6.75% and

4.70% of the SST variance, respectively. The correlation of ECH between PC1 and NINO3 index is 0.96. The correlation is very high, which proves that EOF1 represents the conventional ENSO well in ECH. The correlation of ECH between PC2 and EMI is a low 0.32. The time series of the principal components (PCs) of EOF1, EOF2, EOF3 and EOF4 for the models BCR, CNR, ECH, GFO and, GF1 in DJF SRESA1B are presented in Fig. 5.1 and EMI for the models ECH in DJF of SRESA1B are presented in Fig. 5.2. The model ECO, GFO and GF1 fails to reproduce the ENSO Modoki pattern in DJF as of JJAS for the study period in SRESA1B. The remaining models are not able to reproduce ENSO and ENSO Modoki patterns in DJF for the study period in SRESA1B.

Table 3.2 Categorization of simulated ENSO flavors in 20C3M for boreal winter season (DJF). (* represents ENSO and # represents ENSO Modoki in corresponding mode of EOF).

Models in SRESA1B (DJF)	EOF modes and corresponding variance explained (%)			
	EOF 1	EOF 2	EOF 3	EOF 4
BCR	48.62*	10.90	6.23	5.26
CNR	59.98*	10.89	6.89	3.84
GFO	52.10*	7.34	5.07	4.68 [#]
GF1	51.70*	11.26	6.02	4.08
ECH	50.47*	10.31 [#]	6.75	4.70

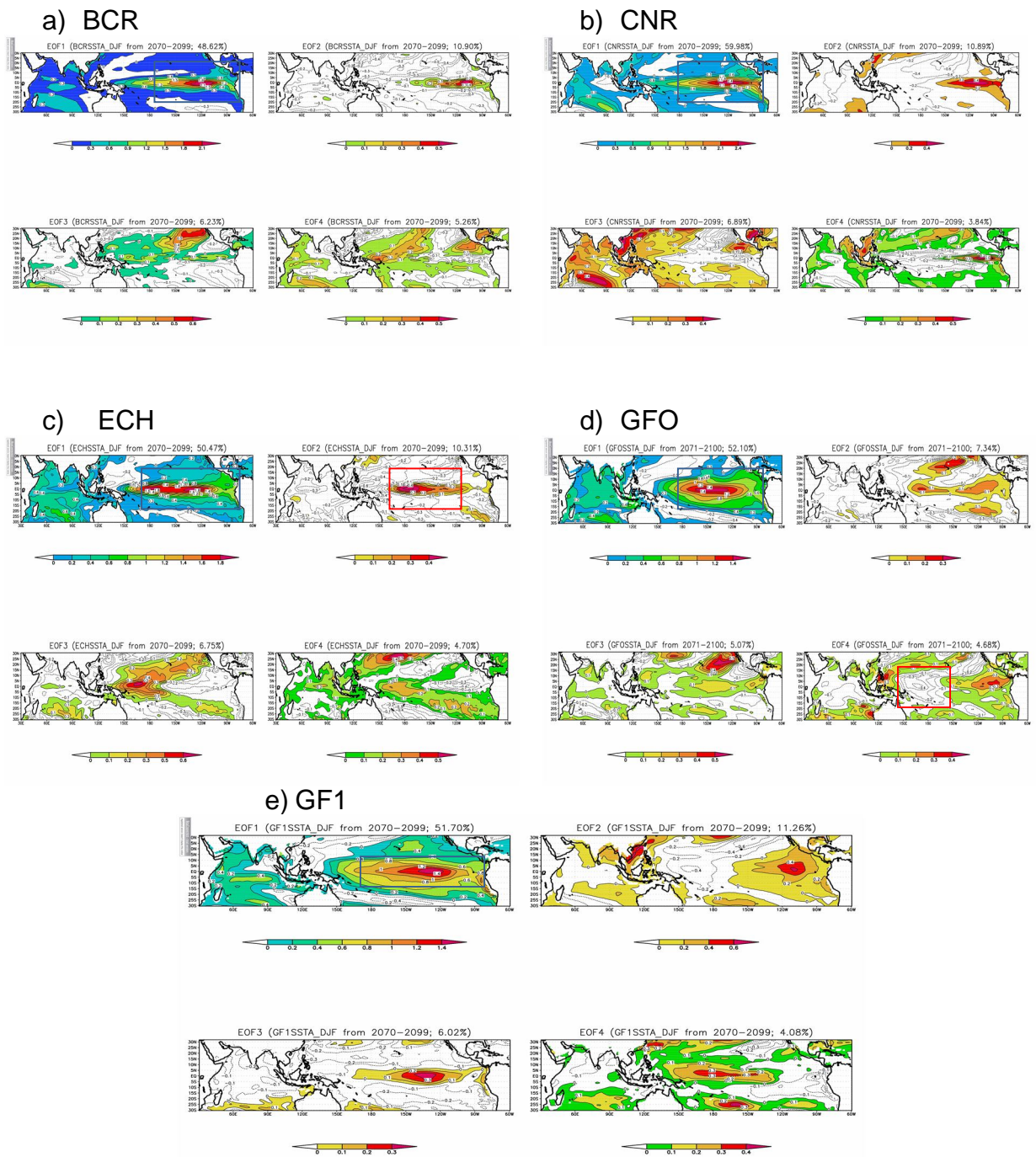


Figure 3.5 Top four EOF modes of SSTA-DJF (SRESA1B) for the models listed in Table 3.2 {Block indicates: Modoki (Red), El Niño (Blue)}.

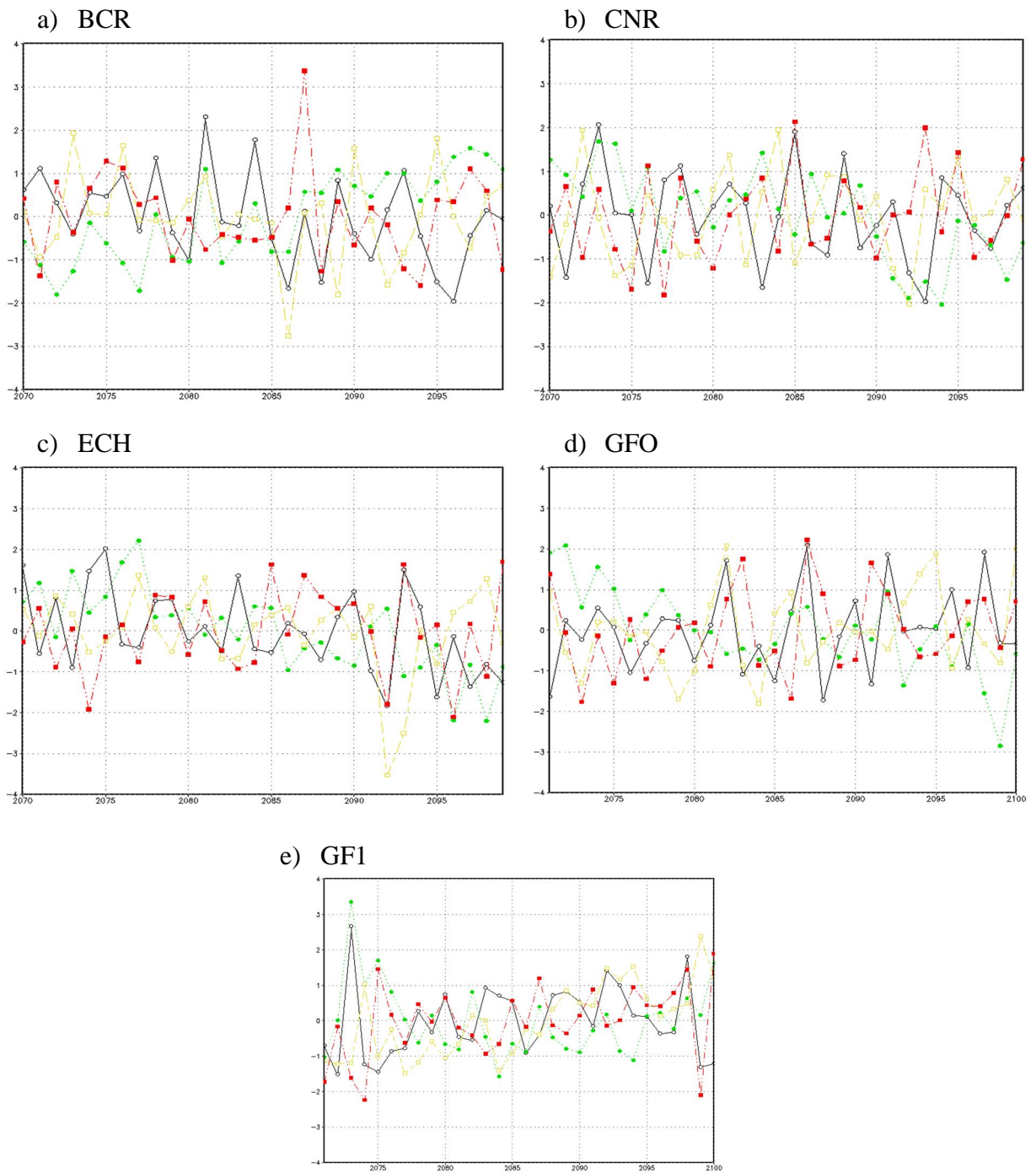


Figure 5.1 Time series of PC1 (solid black), PC2 (dotted green), PC3 (long dash, short dash yellow), PC4 (dot dot dash red) for the models in DJF SRESA1B (a) BCR (b) CNR (c) ECH (d) GFO (e) GF1.

a) ECH

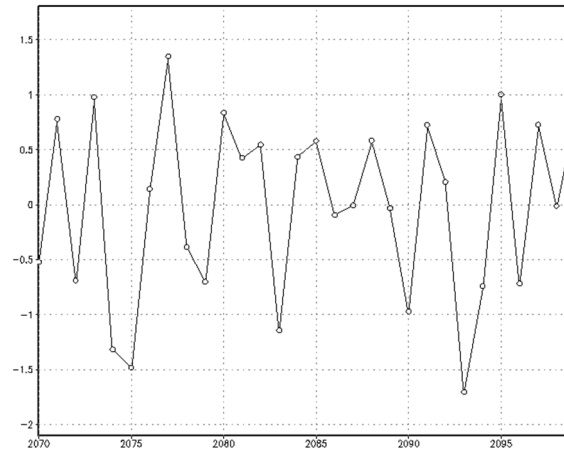


Figure 5.2 Time series of ENSO Modoki index (*standard deviation*) (a) ECH (0.82°C) for DJF in SRESA1B.

3.3) Teleconnections with ISMR

a) Observations and Models in 20C3M

As the ENSO and ENSO Modoki are associated with significant seasonal changes in the tropical SST, it is beneficial to study its teleconnections with Indian Summer Monsoon Rainfall (*Ashok et al., 2007*). Partial correlation technique is adopted (*Pedhazur, 1997; Spiegel, 1997; Ashok et al., 2001, 2003a, b; Saji and Yamagata, 2003; see section 2.3 B*) to study the teleconnections ENSO and ENSO Modoki with ISMR. The JJAS partial correlations of observed data between rainfall anomalies with EMI over the period 1971–2000, after removing the linear influence of NINO3 index is presented in Figure 6a. Figure 6a demonstrates a significant influence of the ENSO Modoki on ISMR. Significant (~ 0.306 at 90% confidence level from a Student's 2-tailed t-test) negative correlations are seen in the parts of western (southern ($r=-0.4$) and northeastern ($r=-0.3$) parts of Indian region. Positive correlations ($r=0.3$) are seen in central- eastern India. Weak positive (negative) correlations are also seen in north (western and northwestern) India. For a comparison, the JJAS partial correlations of NINO3 index with ISMR for the JJAS season are presented in Figure 6b. Significant negative correlations are observed in north and western India.

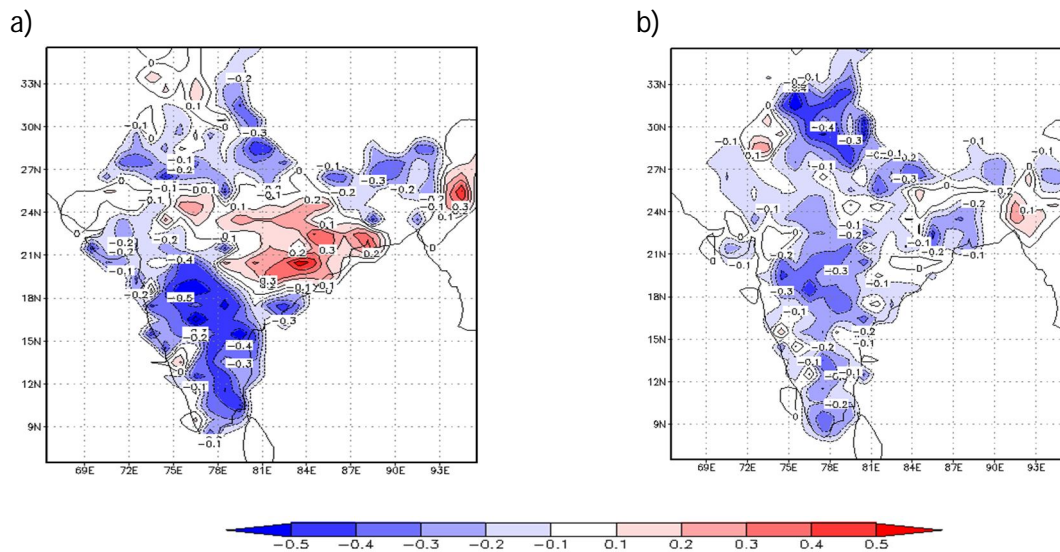


Figure 6 (a) JJAS (1971-2000) partial correlations between observed rainfall anomalies and corresponding EMI (b) Same as Figure 6a but with NINO3 index.

From the Chapter 2, we know that only ING, ECH, GFO and GF1 models reproduce the ENSO and ENSO Modoki-related variance. To evaluate the ability of those models in the in reproducing the Modoki and ENSO impacts on the Indian summer monsoon rainfall, we carry out partial correlation analysis. The impact of ENSO Modoki, for example, is estimated by projecting the simulated summer monsoon rainfall on to the simulated EMI while partialing out the impact from NINO3 index for the period of last thirty years in 20C3M.

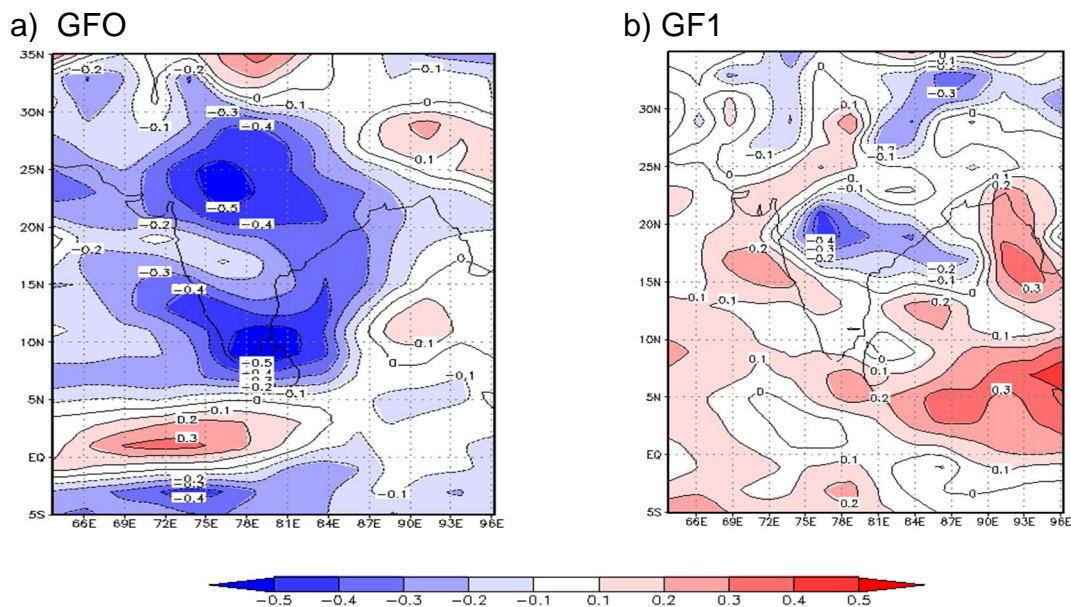


Figure 7 Partial correlations between rainfall anomalies and EMI (a) GFO (b) GF1 for JJAS in 20C3M.

The JJAS partial correlations computed between the EMI and rainfall anomalies for the models GFO and GF1 are shown in Figs. 7a and 7b. The corresponding JJAS partial correlations computed between the NINO3 index and rainfall anomalies after removing the influence of EMI for the models GFO and GF1 are shown in Figs. 8a and 8b. The model GFO (Fig. 7a) successfully captures the observed negative correlations between the ISMR and EMI, over the South India but fails to capture the positive correlations further north. However, the signs of the partial correlation of the EMI with ISMR as simulated by the model GF1 (Fig. 7b) is opposite that from observations (Fig. 7a). Fig. 8 demonstrates the simulated influence of the ENSO on ISMR in the above two models. The results from GF1 shows (Fig. 8a) unrealistic strong positive correlations from central to north of India. The model GFO (Fig. 8b), on the other hand, shows realistically signed, but stronger than observed, ENSO impacts on ISMR.

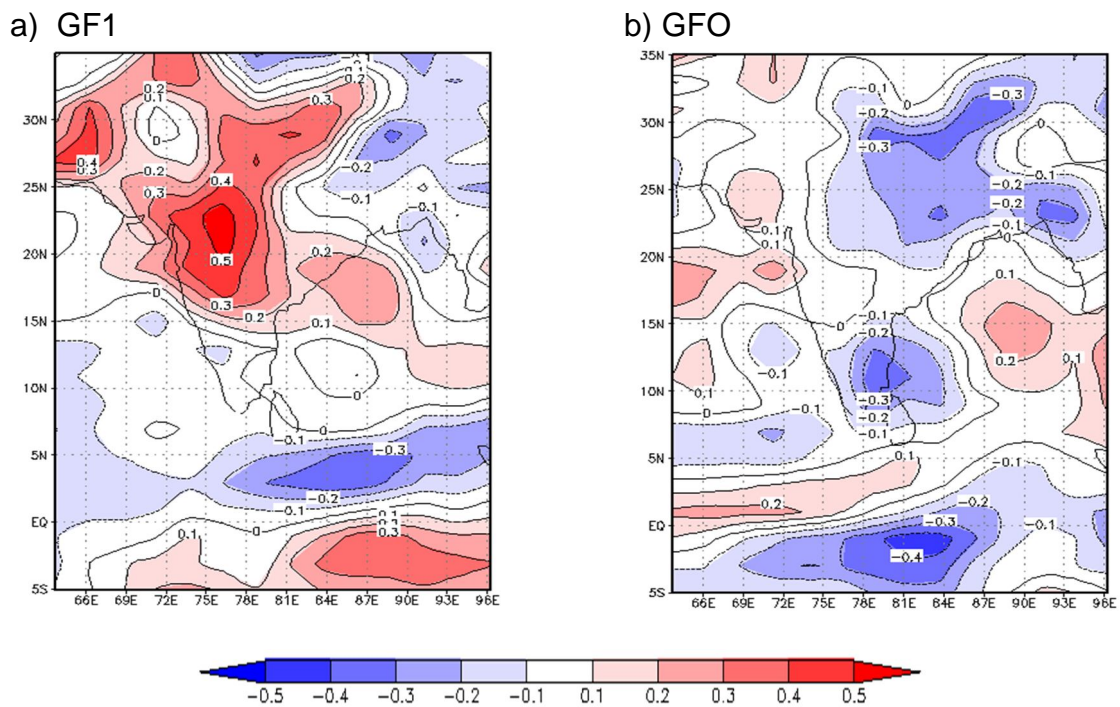


Figure 8 Same as Figure 7 but with NINO3 index (a) GF1 (b) GFO for JJAS in 20C3M.

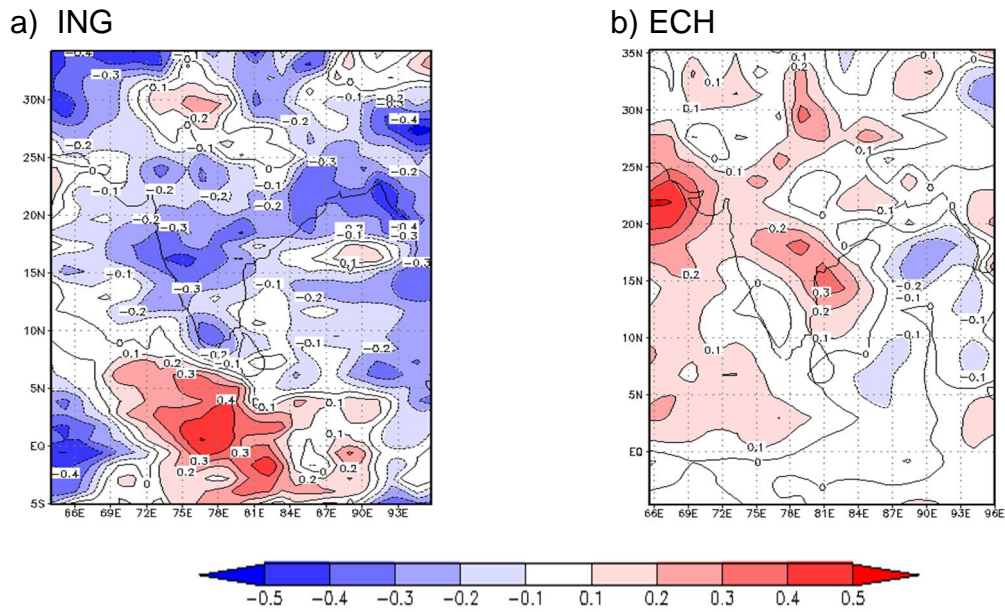


Figure 9 Partial correlations between rainfall anomalies and NINO3 index (a) ING (b) ECH for JJAS in 20C3M.

The JJAS partial correlations computed between the NINO3 index and rainfall anomalies after removing the influence of EMI for the models ING and ECH, those models that are able to simulate only ENSO, are shown in Figs. 9a and 9b. Most parts of the Indian regions have negative correlation ($r=-0.3$; *ING*; *Fig. 9a*) as observations (*Fig. 6b*). The ECH model shows positive correlations, as opposite to the negative observations (*Fig. 6b*).

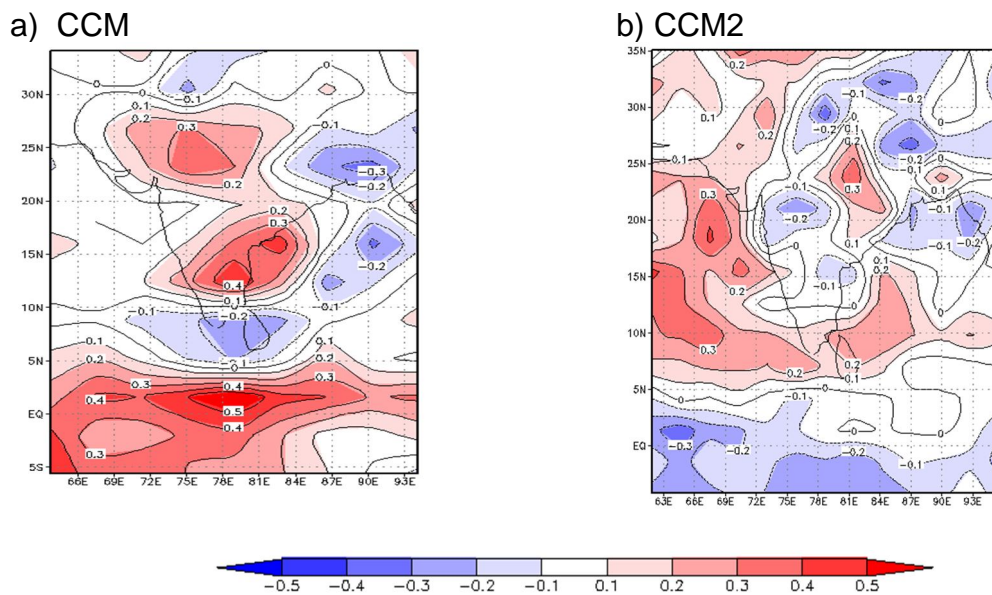


Figure 10 Partial correlations between rainfall anomalies and EMI (a) CCM (b) CCM2 for JJAS in 20C3M.

The JJAS partial correlations computed between the EMI and rainfall anomalies after removing the influence of NINO3 index for the models BCR and CNR, which are able to simulate only ENSO Modoki, are shown in Figs. 10a and 10b. The correlations patterns are oppositely signed (*Fig. 10a*) as compared to that in the observations in northern and central part of India the model CNR (*Fig. 10b*) shows negative correlations as that of observations (*Fig. 6a*), but the magnitude of the simulated correlations, in general, is weak.

b) Projections in SRESA1B scenario

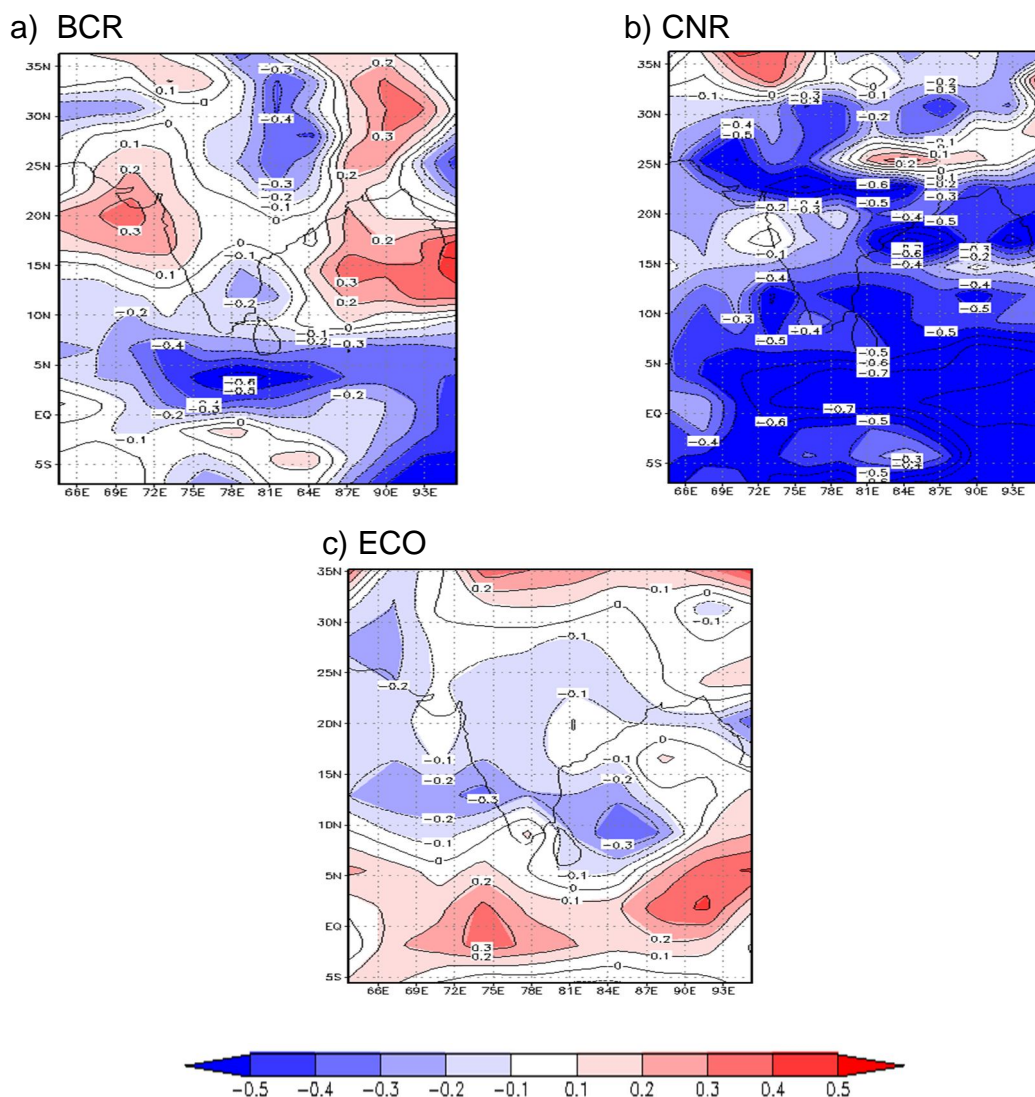


Figure 11 Partial correlations between rainfall anomalies and NINO3 index (a) BCR (b) CNR for JJAS and (c) ECO for JJAS but with EMI in SRESA1B.

To investigate the influence of climate change on the ENSO/ENSO Modoki – ISMR relationship, projected changes in seasonal precipitation under the climate change experiment SRESA1B is examined using partial correlation techniques. The JJAS partial correlations computed between the NINO3 index and rainfall anomalies for the models BCR and CNR are shown in Figs. 11a and 11b. The model BCR (Fig. 11a) and CNR (Fig. 11b) shows the ENSO impact over India in boreal summer season as of observations. The JJAS partial correlation computed between the EMI and rainfall anomalies of the model ECO are shown in Fig. 11c. The model ECO (Fig. 11c) has negative correlations as of observations (Fig. 6a) in many parts of Indian region indicate the signal of drought.

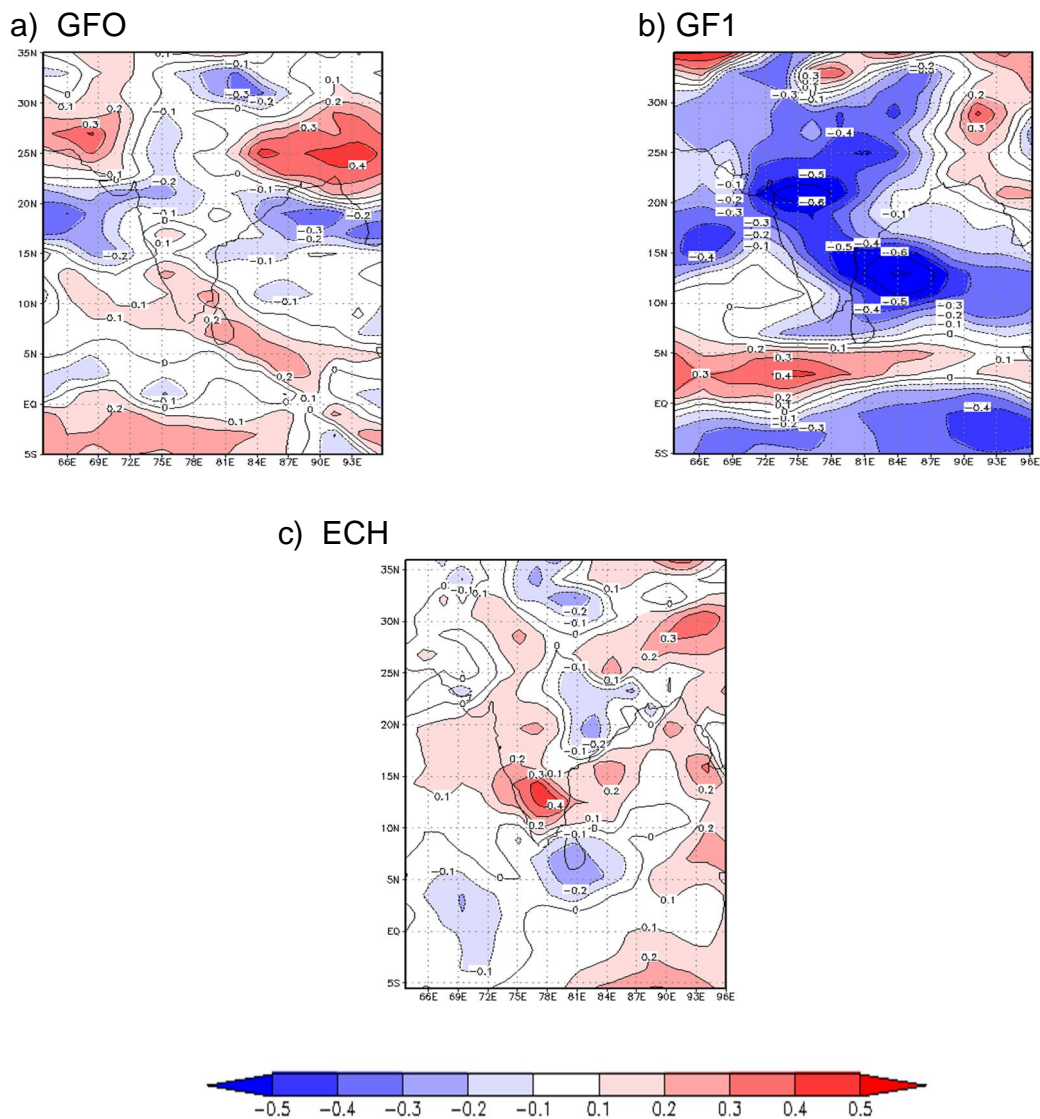


Figure 12 Partial correlations between rainfall anomalies and NINO3 index (a) GFO (b) GF1 (c) ECH for JJAS in SRESA1B.

The JJAS partial correlations computed between the NINO3 and rainfall anomalies for the models GFO, GF1 and ECH are shown in Figs. 12a, 12b and 12c. The model GFO (Fig. 12a) represents positive correlations in northeast of India, which indicates surplus rainfall over that region. The west coast, central, southern and eastern parts of India shows the influence of ENSO. The model GF1 (Fig. 12b) represents negative correlations ($r=-0.5$) in central to southern part of India indicates the drought in that region. The model ECH (Fig. 12c) represents positive correlations in northeast and south of India will have significant rainfall.

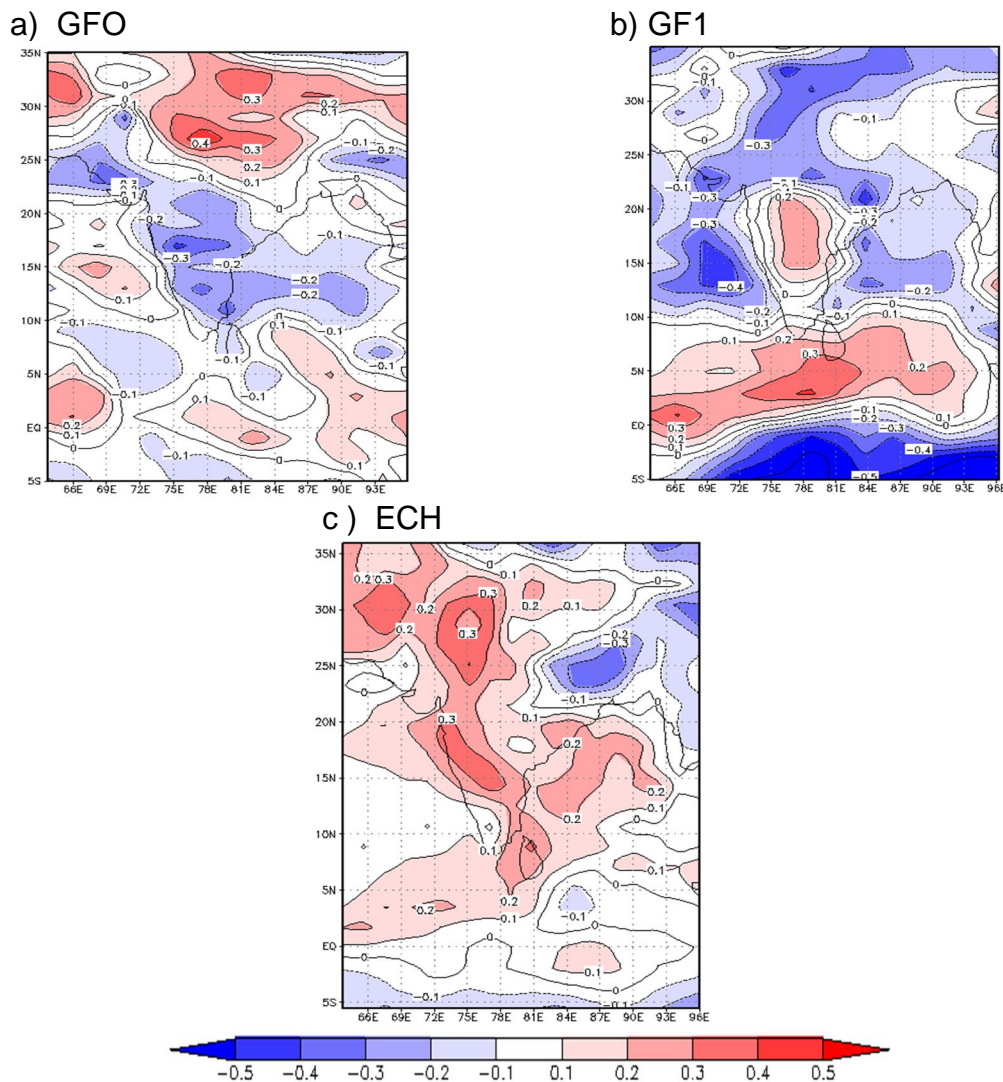


Figure 13 Same as Figure 12 but with EMI (a) GFO (b) GF1 (c) ECH for JJAS in SRESA1B.

The JJAS partial correlations computed between the EMI and rainfall anomalies for the models GFO, GF1 and ECH for the study period in SRESA1B are shown in Figs. 13a, 13b and 13c. The model GFO (Fig. 13a) represents positive correlations over

north and northeast of India and negative correlations over southern part of Indian region. The ENSO Modoki and ISMR relationship is well simulated by the model GF1 and ECH in many parts of India (*Fig. 13b and c*).

4. SUMMARY AND CONCLUSIONS

Data from the observations, and that from the 20C3M and SRESA1B climate change runs from the IPCC AR4 were analyzed to study whether the IPCC climate models can reproduce the ENSO and ENSO Modoki patterns as the gravest two modes from statistical linear analysis, as observed, and their teleconnections with the Indian summer monsoon, and also the implications for the future.

An EOF analysis of the observational SST anomalies in the tropical Pacific shows that the El Niño and El Niño Modoki explain 45% and 13% of the tropical Pacific SST variance respectively for the boreal summer season during the period from 1971 through 2000, in broad agreement with Ashok et al., (2007). To see whether the models reproduce this variability, EOF analysis has been carried out on simulated SSTA data from the 20C3M for the last 30 years of twentieth century. Based on the results, the CMIP3 models are separated into 3 groups: one that captures both ENSO and ENSO Modoki, and the second group that reproduces only either the ENSO or ENSO Modoki mode (*Table 4.1*), and the third group which fails to reproduce any of these top two modes (*see chapter 3*). This grouping information helps to determine which CMIP3 models should be used to understand the fidelity of the simulated ENSO and ENSO Modoki.

It is found that only 25% of the models from 20C3M capture either ENSO or ENSO Modoki pattern in JJAS (*Fig. 3.2; Table 2.1*) and DJF (*Fig. 3.3; Table 2.2*). It is to be noted however, that even in the models with “better” capability, the latitudinal width of the captured modes differs from that of the observations, and sometimes, the number of the mode as well. For the JJAS season, only 2 out of the 23 models, namely ING and ECH (*Fig. 3.2a, b*), capture the ENSO. The CCM and CCM2 (*Fig. 3.2c, d*) models are able to capture ENSO Modoki. Only the two models GFO and GF1 (*Fig. 3.2e, f*) simulate both ENSO and ENSO Modoki as important modes. On the other hand, for the corresponding DJF season, only 3 out of the 23 models, namely ING, ECH and GF1 (*Fig. 3.3a, b and e*) capture ENSO. The CCM2 model is able to capture (*Fig. 3.3c*) ENSO Modoki. Only one model GFO (*Fig. 3.3d*) simulates both ENSO and ENSO Modoki as important modes.

Table 4.1: Categorization of simulated ENSO flavors in 20C3M and SRESA1B for boreal summer (JJAS) and boreal winter (DJF) season. Numbers in parenthesis indicates the corresponding modes of EOF. Further, in parenthesis of row 3, E and M represents the ENSO and ENSO Modoki.

Models reproduces	20C3M (JJAS)	20C3M (DJF)	SRESA1B (JJAS)	SRESA1B (DJF)
Only ENSO	ING (1); ECH (1)	ING (1); GF1 (1); ECH (1)	BCR (1); CNR (1)	BCR (1); CNR (1); GF1 (1)
Only ENSO Modoki	CCM (4); CCM2 (3)	CCM2 (4)	ECO (3)	-----
Both ENSO & ENSO Modoki	GFO (1E & 4M); GF1 (1E & 2M)	GFO (1E & 2M)	GFO (1E & 2M); GF1 (1E & 2M); ECH (1E & 2M)	GFO (1); ECH (1E& 2M)

In summary, only the GFO model captures both the Modoki and ENSO modes realistically for boreal summer as well as boreal winter during the last 30 years of the 20C3M.

It is also found that only 20% of the models from SRESA1B capture either ENSO or ENSO Modoki pattern to some extent similar to the observations (*Fig. 3.1*) during JJAS (*Fig. 3.4; Table 3.1*) and DJF (*Fig. 3.5; Table 3.2*). Further, just as in 20C3M simulations, the latitudinal width of these captured modes differs from that of the observations. For the JJAS season only 2 out of the 23 models, namely BCR and CNR (*Fig. 3.4a, b*) capture ENSO. The model ECO (*Fig. 3.4c*) is able to capture ENSO Modoki and three models ECH, GFO and GF1 (*Fig. 3.4d, e and f*) simulate both ENSO and ENSO Modoki. Analysis of the corresponding boreal winter simulations shows that only 4 out of the 23 models, namely BCR, CNR, GFO and GF1 (*Fig. 3.5a, b, d and e*) capture ENSO.

Ashok et al. (2009) suggested that the frequent occurrence of the El Niño Modoki events since late 1970s is due to global warming. Yeh et al. (2009) analyzed the SREA1B and 20C3M outputs and suggest that the ENSO Modoki events may increase in a global warming condition. However, the current analysis does not support the finding of Yeh et al (2009). For example, the variances explained by

simulated ENSO Modoki by the model GFO (GF1), which captures both El Niño and El Niño Modoki, decreases (increases) in SRESA1B as compared to the corresponding variance in 20C3M run, indicating a disagreement between the two models. In addition, the ENSO-associated variance in fact decreases from boreal summer to winter in 20C3M in contrast to observations in the GFO and GF1 models, indicating a systematic bias in the model simulations of ENSO-associated variance. Similar reduction is also simulated in the corresponding SREA1B simulations, hinting that this may be due to the systematic bias.

Observational analysis (*Fig. 3.6a and b*) for the period 1971-2000 shows that the ENSO Modoki has stronger impact as compared to that of the ENSO, in agreement with Ashok et al. (2007) and Kumar et al. (2006). Interestingly, Kriplani et al. (2007) and Sabade et al. (2010), based on the IPCC data analysis, broadly suggest that the monsoon-ENSO relationship does not change noticeably. Our study examines this issue from the perspective of the two dominant tropical Pacific drivers, namely, ENSO and ENSO Modoki. We, however, are unable to come to any specific conclusion in this regard, given the diverse results, and also the limited skills of the models in reproducing the monsoon, the ENSO and ENSO Modoki. From the Table 2.1 of the Section 3, it is deciphered that the two models that reproduce ENSO Modoki as well as ENSO associated variance in both 20C3M and SRESA1B represent the links of the ISMR with ENSO reasonably in 20C3M, but indicate opposite type of impacts in SREA1B. It is difficult to reconcile that the teleconnections of a tropical driver can change like that. The GF1, ECO etc. express the expected negative impacts from tropical Pacific in SREA1B scenarios, but they are either unable to reproduce the observed links during the 20th century. All this indicates the challenges associated with the limitations of the models in reproducing the variability of the monsoons and ENSO flavors, not to speak of failing in capturing the potential impacts of global warming as they are expected to. More research in improving the current day simulations, improving model capacity to simulate better by improving the Green House Gases (GHG) and aerosols in the models are some of the important and immediate steps that are necessary.

5. REFERENCES

- Ashok, K., Z. Guan and T. Yamagata, 2001: Impact of the Indian Ocean Dipole on the relationship between the Indian Monsoon rainfall and ENSO. *Geophys. Res. Lett.* 26, 4499-4502.
- Ashok, K., Z. Guan and T. Yamagata, 2003b: Influence of the Indian Ocean dipole on the Australian winter rainfall. *Geophys. Res. Lett.*, 30(15), 1821, doi: 10.1029/2003GL017926.
- Ashok, K., Z. Guan and T. Yamagata, 2003a: A look at the relationship between the ENSO and the Indian Ocean dipole *J. Met. Soc. Japan*, 81, 41-56.
- Ashok, K., H. Weng, S. Behera, S. A. Rao, and T. Yamagata, 2007: El Niño Modoki and its teleconnection, *J. Geophys. Res.*, 112, C11007, doi: 10.1029/2006JC003798.
- Ashok, K., and T. Yamagata, 2009: The El Niño with a difference? *Nature*, (Invited News & Views piece), 461, 481-484 (24 September 2009) doi: 10.1038/461481a; Published online 23 September 2009.
- Aceituno, P. (1988), on the functioning of the Southern Oscillation in the South American sector, Part I: Surface climate, *Mon. Weather Rev.*, 116, 505– 525.
- Diaz h, martin p. Hoerling and jon k. Eischeid; enso variability, teleconnections and climate change; *int. J. Climatol.* 21: 1845–1862 2001, doi: 10.1002/joc.631.
- Kumar K K, Rajagopalan B and Cane M A 1999: On the weakening relationship between the Indian monsoon and ENSO; *Science* 284 2156–2159.
- Kripalani R. H. and Ashwini Kulkarni (1997) Climatic impact of El Niño / La Niña on the Indian monsoon: A new perspective *Weather* 52: 39-46.

Kumar, K., B. Rajagopalan, M.Hoerling, G.Bates and M.Cane, 2006, Science. Unraveling the Mystery of Indian Monsoon Failure during El Niño, doi: 10.1126/science.1131152.

Lorenz, E. N., (1956): Empirical orthogonal functions and statistical weather prediction. Sci. Rep. No. 1, Statistical Forecasting Project, M.I.T., Cambridge, MA, 48 pp.

Levitus, S., J. Antonov, and T. Boyer (2005), Warming of the world ocean, 1955 – 2003, Geophys. Res. Lett., 32, L02604, doi: 10.1029/2004GL021592.

Meehl GA, Covey C, Delworth T, Latif M, McAvaney B, Mitchell JFB, Stouffer RJ, Taylor KE (2007) The WCRP CMIP3 multimodel dataset. A new era in climate change research. Bull Am Meteorol Soc 88:1383–1394.

Philander, S. G. H., (1990): El Niño, La Niña, and the Southern Oscillation. Academic Press.

Pedhazur, E. J. (1997), Multiple Regressions in Behavioural Research: Explanation and Prediction, 3rd ed., Holt, Rinchart, and Winston, Austin, Tex.

R H Kripalani, J H Oh, Ashwini Kulkarni, S S Sabade and H S Chaudhari (2006) South Asian Summer monsoon precipitation variability: Coupled climate model simulations and projections under IPCC AR4. Theor Appl Climatol, 90, 133-159.

Rayner, N. A., D. E. Parker, E. B. Horton, C. K. Folland, L. V. Alexander, D. P. Rowell, E. C. Kent, and A. Kaplan (2003), Global analyses of sea surface temperature, sea ice, and night marine air temperature since the late nineteenth century, J. Geophys. Res., 108(D14), 4407, doi: 10.1029/2002JD002670.

Rajeevan, M., Bhate, J., Kale, J.D. and B. Lal, 2006, High resolution daily gridded rainfall data for the Indian region: Analysis of break and active monsoon spells, Current Science, 91, 3, 296 – 306.

Rasmusson, E. M., and T. H. Carpenter, 1982: Variations in tropical sea surface temperature and surface wind fields associated with the Southern Oscillation/El Niño. *Mon. Wea. Rev.*

Ropelewski C F and Halpert M S 1987 Global and regional scale precipitation patterns association with El Niño/southern oscillation; *Mon. Weather Rev.* 1151606–1626.

Rayner, N. A., D. E. Parker, E. B. Horton, C. K. Folland, L. V. Alexander, D. P. Rowell, E. C. Kent, and A. Kaplan (2003), Global analyses of sea surface temperature, sea ice, and night marine air temperature since the late nineteenth century, *J. Geophys. Res.*, 108(D14), 4407, doi: 10.1029/2002JD002670.

Sabade S. S & Ashwini Kulkarni & R. H. Kripalani (2010): Projected changes in South Asian summer monsoon by multi-model global warming experiments, *Theor Appl Climatol*, DOI 10.1007/s00704-010-0296-5

Saji N H and Yamagata T 2003: Possible impacts of Indian Ocean dipole mode events on global climate; *Clim. Res.*25 151–169.

Spiegel, M. R. (1997), *Schaum's Outline of Theory and Problems of Statistics*, McGraw-Hill, New York.

Trenberth, K. E., and T. J. Hoar, 1997: El Niño and climate change. *Geophys Res Let.*

Trenberth, K. E., Branstator, G. W., Karoly, D., Kumar, A., Lau, N.-C. and Ropelewski, C (1998). Progress during TOGA in understanding and modeling global teleconnections associated with tropical sea surface temperatures. *J. Geophys. Res.*103, 14291-14324.

Trenberth, K. E., D. P. Stepaniak, J. W. Hurrell, and M. Fiorino (2001), Quality of reanalyses in the tropics, *J. Clim.*, 14, 1499– 1510.

Yeh et al., 2009: El Niño in a changing climate, *Nature* 461, 511-514 (24 September 2009) | doi: 10.1038/nature08316.